J. Fluid Mech. (2000), *vol.* 425, *pp.* 335–366. Printed in the United Kingdom

Theoretical and computational aspects of the self-induced motion of three-dimensional vortex sheets

By C. POZRIKIDIS

Department of Mechanical and Aerospace Engineering, University of California,
San Diego, La Jolla, California 92093-0411, USA
cpozrikidis@ucsd.edu

(Received 24 May 1999 and in revised form 22 June 2000)

Theoretical and computational aspects of the self-induced motion of closed and periodic three-dimensional vortex sheets situated at the interfaces between two inviscid fluids with generally different densities in the presence of surface tension are considered. In the mathematical formulation, the vortex sheet is described by a continuous distribution of marker points that move with the velocity of the fluid normal to the vortex sheet while executing an arbitrary tangential motion. Evolution equations for the vectorial jump in the velocity across the vortex sheet, the vectorial strength of the vortex sheet, and the scalar circulation field or strength of the effective dipole field following the marker points are derived. The computation of the self-induced motion of the vortex sheet requires the accurate evaluation of the strongly singular Biot-Savart integral whose existence requires that the normal vector varies in a continuous fashion over the vortex sheet. Two methods of computing the principal value of the Biot-Savart integral are implemented. The first method involves computing the vector potential and the principal value of the harmonic potential over the vortex sheet, and then differentiating them in tangential directions to produce the normal or tangential component of the velocity, in the spirit of generalized vortex methods developed by Baker (1983). The second method involves subtracting off the dominant singularity of the Biot-Savart kernel and then accounting for its contribution by use of vector identities. Evaluating the strongly singular Biot-Savart integral is thus reduced to computing a weakly singular integral involving the mean curvature of the vortex sheet, and this allows the routine discretization of the vortex sheet into curved elements whose normal vector is not necessarily continuous across the edges, and the computation of the self-induced velocity without kernel desingularization. Numerical simulations of the motion of a closed or periodic vortex sheet immersed in a homogeneous fluid confirm the effectiveness of the numerical methods for a limited time of evolution. Numerical instabilities arise after a certain evolution time due to the ill-posedness of vortex sheet dynamics. The motion may be regularized by desingularizing the Biot-Savart kernel using either Krasny's (1986*b*) method or spectrum truncation. Depending, however, on the physical mechanism that drives the motion, the instabilities may persevere.

1. Introduction

A vortex sheet is a mathematical idealization of a homogeneous fluid layer, or a heterogeneous layer straddling the interface between two different fluids, across which the magnitude and possibly the direction of the velocity changes rapidly between two different values. As the thickness of the vortex layer tends to zero while the jump in the velocity is held constant, a surface of discontinuity arises and is identified as a vortex sheet. In reality, the notion of a vortex sheet whose thickness is and remains infinitesimal at all times is acceptable only in the context of inviscid flow. In the presence of viscosity, tangential stresses cause the singular vorticity distribution supported by the vortex sheet to instantaneously spread out, smearing the discontinuity. Notwithstanding this physical limitation, vortex sheets are of interest for two main reasons. First, they provide us with convenient computational models for studying the dynamics of a class of vortex flows at high Reynolds numbers, at scales that are larger than an appropriate inverse power of the Reynolds number defined with respect to the instantaneous thickness of a vortex layer. Second, the study of vortex sheet dynamics allows us to develop insight into the analytical structure of solutions of the Euler equations associated with self-induced vortex motion. The general subject of vorticity dynamics and vortex methods has been reviewed by Leonard (1985), Saffman (1992), and Puckett (1993).

Following Rosenhead's (1931) point vortex approximation, several numerical methods have been developed for simulating the exact or regularized self-induced motion of vortex sheets in two dimensions. Unfortunately, the generalization of the point vortex method to axisymmetric or genuine three-dimensional flows is prohibited by an intrinsic difficulty: the low-order discretization of a curved vortex sheet produces either vortex rings and curved vortex lines with unbounded self-induced velocities, or vortex particles whose induced velocity does not describe solutions of the Euler equations even in a weak sense of the term. As a remedy, the motion may be regularized by arbitrarily or judiciously assigning non-zero size to the vortex core, thus obtaining vortex blobs. To study the behaviour of a true vortex sheet, however, the limit of vanishing core size must be taken simultaneously with the limit of an increasingly refined discretization. An alternative is to use a higher order spatial discretization, thereby maintaining the continuity of the singular vortex sheet. Agishtein & Migdal (1989) and Caflisch, Li & Shelley (1993) implemented discretizations based on B-splines or quartic spline interpolation for axisymmetric flows.

Because of the failure of computational models based on low-order discretization, a numerical method for computing the self-induced motion of three-dimensional vortex sheets must necessarily incorporate three features. First, the geometry of the vortex sheet must be described in global or local parametric form by high-order interpolation or approximation. Second, the principal value of the Biot-Savart integral must be computed with sufficient accuracy. Third, the evolution equations of the variables defining the shape of the vortex sheet, such as the position of nodes that define surface elements, and the vorticity transport equation governing the strength of the vortex sheet or circulation along a contour that pierces the vortex sheet at two specified points, must be integrated in time using numerical methods.

Agishtein & Migdal (1989) implemented a numerical procedure that discretizes a vortex sheet into flat triangles defined by three vertices. Brady, Leonard & Pullin (1998) implemented an adaptive discretization into cubic Bѐzier triangular patches whose collection comprises a smooth surface with continuous normal vector. Lozano, Garcìa-Olivares & Dopazo (1998) considered the flow induced by a doubly periodic vortex sheet and implemented a discretization into rectangular patches. In these computational studies, the principal value of the Biot-Savart integral was computed by first desingularizing its strongly singular kernel using a variant of the δ-method introduced by Krasny (1986*b*) for two-dimensional flow, and then applying fixed or adaptive numerical integration quadratures. Now, as the size of the regularization parameter δ is reduced, the integration methods become increasingly ineffective or else inaccurate, eventually leading to failure. Thus, even the instantaneous self-induced velocity field associated with a specified vorticity distribution cannot be computed.

With the exception of the recent work of Haroldsen & Meiron (1998) discussed in the next paragraph, a numerical method for the direct evaluation of the principal value of the Biot-Savart integral over a discretized three-dimensional vortex sheet without kernel regularization has not been developed. The main difficulty is that the Biot-Savart kernel exhibits a strong $1/r^2$ singularity; as a consequence, the principal value of the integral exists only when the normal vector varies over the vortex sheet in a continuous fashion. In contrast, the kernel of the double-layer harmonic potential diverges only weakly as $1/r$, and the principal value of the integral exists even on a discontinuous surface. The requirement on geometrical smoothness appears to invalidate the local discretization of vortex sheets into flat or curved elements with edge discontinuities in the normal vector, and this considerably complicates the implementation of numerical methods. We shall see, however, that a judicious method of reducing the order of the singularity by use of integral identities circumvents this essential difficulty and allows the implementation of standard boundary element methods.

Haroldsen & Meiron (1998) developed a method for computing the principal value of the Biot-Savart integral over a doubly periodic vortex sheet using the modified double trapezoidal rule on a rectangular grid, where the singular contribution is excluded from the summation. Their error analysis shows that the trapezoidal approximation introduces an error that may be expressed as a series of odd powers of the grid size, starting with the first power. With 32 divisions in each direction, corresponding to 1024 surface patches, the relative error is on the order of 10%, which is substantial. The repetitive application of Richardson extrapolation allows significant improvements, but the additional CPU and logistical effort discourages the use of the method for carrying out dynamical simulations. In contrast, the single application of Richardson extrapolation to the corresponding point vortex approximation of a vortex sheet in two dimensions yields a spectrally accurate method (Shelley 1992). This fundamental difference in the behaviour of the error underlines the importance of maintaining the continuity of vortex lines in the numerical approximation.

Baker, Meiron & Orszag (1982) and Baker (1983) developed generalized vortex methods for interfacial flow whose distinguishing feature is that the flow is represented by a distribution of potential dipoles oriented normally to the vortex sheet. The strength of the dipoles is equal to the circulation along a closed contour that pierces the vortex sheet through a fixed and a variable marker or Lagrangian point. In the generalized vortex method, the principal value of the Biot-Savart integral is computed by evaluating the vector potential and principal value of the harmonic potential over the vortex sheet, and then differentiating them in tangential directions to produce the normal or tangential component of the velocity. Baker, Meiron & Orszag (1984) implemented and demonstrated the success of the method for axisymmetric flow, and Baker & Moore (1989) studied its performance in comparison with the point vortex method for two-dimensional flow.

In this work, we implement numerical methods for the direct or indirect evaluation of the Biot-Savart integral for three-dimensional flow based on conventional surface triangulation into curved quadratic elements, accompanied by isoparametric interpolation. The Biot-Savart integral, vector potential, and principal value of the harmonic potential are evaluated in terms of surface integrals exhibiting a strong or weak singularity. The former is subtracted off by use of an integral identity, and the latter is handled by integrating in local curvilinear coordinates using the polar integration rule. The new methodology allows the efficient computation of the self-induced velocity without kernel desingularization. When a vortex sheet is discretized into 512 elements, the relative error in the computation of the Biot-Savart integral is on the order of 0.1%, which is at least two orders of magnitude less than that corresponding to the trapezoidal discretization (Haroldsen & Meiron 1998). The accuracy of the numerical method is found to be adequate for dynamical simulations with a modest number of elements, but regularization is necessary for suppressing inherent instabilities encountered in vortex sheet dynamics.

To compute the evolution of a three-dimensional vortex sheet, we require evolution equations for the strength of the vortex sheet or circulation field over the vortex sheet. Several authors have shown that, in the case of a vortex sheet embedded in a homogeneous fluid, the circulation along a closed contour that pierces the vortex sheet at two specified marker points moving with the principal velocity of the vortex sheet remains constant in time (Caflisch 1988; Agishtein & Migdal 1989). Corresponding equations for vortex sheets separating fluids with different densities in the presence of surface tension have been derived by Wu (1995) and Lozano *et al.* (1998), although certain discrepancies exist in the final forms of their equations. The properties of the integral equations for the rate of change of the strength of the vortex sheet have not been discussed in detail by previous authors.

In this paper, several contributions to the theory and computation of the self-induced motion of three-dimensional vortex sheets are made. First, a comprehensive set of equations governing the motion of closed or periodic three-dimensional vortex sheets, regarded as the interfaces between two inviscid fluids in the presence of surface tension, is presented. Second, the properties of the integral equations for the rate of change of the jump in the velocity across the vortex sheet, the strength of the vortex sheet, and the circulation or strength of the effective dipole distribution are discussed. Third, numerical methods for describing the motion of vortex sheets based on standard boundary element methods are developed. Fourth, numerical methods for computing the principal value of the Biot-Savart integral based on vortex sheet triangulation using conventional or generalized vortex methods are compared. Finally, representative simulations of the motion of vortex sheets immersed in homogeneous fluids are presented.

Describing evolving surfaces by triangulation is now a standard choice in various fields of interfacial dynamics, as reviewed by Pozrikidis (2000*b*), and the developments in this work highlight the problem of vortex sheet dynamics against the more general framework of the dynamics of advancing fronts. Overall, this work offers extensions of the mature field of vortex sheet dynamics in two dimensions to its more challenging and much less studied counterpart for three-dimensional flow.

2. Vortex sheet kinematics

Consider a three-dimensional closed, singly or doubly periodic vortex sheet separating two inviscid fluids, as depicted in figure 1, possibly in the presence of an impenetrable surface that conforms with the periodicity of the flow, not shown in the figure. We denote the designated exterior or upper, and interior or lower, side of the vortex sheet, respectively, by the subscript or superscript + or −, and introduce the unit vector $\boldsymbol{n}$ that is normal to the vortex sheet and points into the exterior fluid labeled +, as shown in figure 1. In the case of doubly periodic flow depicted

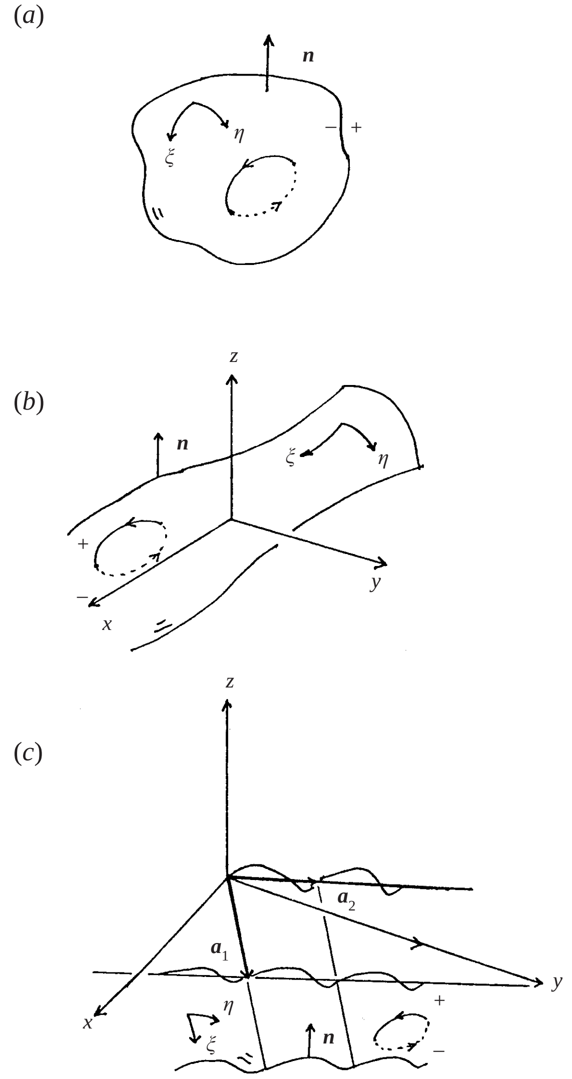

FIGURE 1. Schematic illustration of (*a*) a closed, (*b*) a singly periodic, and (*c*) a doubly periodic vortex sheet. The vortex sheet marks the interface between two inviscid fluids with generally different densities, in the presence of surface tension.

in figure 1(*c*), the periodicity of the vortex sheet is described by the two arbitrary base vectors $\boldsymbol{a}_1$ and $\boldsymbol{a}_2$, so that any doubly periodic scalar, vectorial, or higher-order geometrical or flow variable q satisfies the periodicity condition $q(\boldsymbol{x}) = q(\boldsymbol{x}+\boldsymbol{X}_n)$. The points $\boldsymbol{X}_n$ define the vertices of a planar lattice parallel to the (x, y)-plane, located at $\boldsymbol{X}_n = i_1\boldsymbol{a}_1 + i_2\boldsymbol{a}_2$, where i_1 and i_2 are two integers.

The vortex sheet separates two immiscible inviscid fluids with densities ρ^+ and ρ^-, with the interface exhibiting constant and uniform surface tension T. In the absence of viscous stresses, a force balance over an infinitesimal control volume enclosing a small section of the interface requires that the pressure p undergo a discontinuity across the vortex sheet given by

$$p^- - p^+ = T\ 2\kappa_m \qquad (2.1)$$

where $\kappa_m = \frac{1}{2}\nabla \cdot \boldsymbol{n}$ is the mean curvature of the interface. In the absence of interfacial tension, the pressure and thus its tangential gradient is continuous across the interface, but the normal derivative is generally discontinuous.

By definition, the normal component of the fluid velocity is continuous across the vortex sheet, but the tangential component undergoes a discontinuity defined as

$$\Delta \boldsymbol{u} \equiv \boldsymbol{u}^{+} - \boldsymbol{u}^{-}. \tag{2.2}$$

The velocity field on either side of the vortex sheet may be decomposed into a continuous, generally rotational component denoted by $\boldsymbol{u}^{\infty}$, and a non-analytic irrotational component associated with the discontinuity represented by the vortex sheet, denoted by $\boldsymbol{u}^{VS}$. Expressing the velocity of the irrotational component on either side of the vortex sheet in terms of a harmonic potential, we find

$$\Delta \boldsymbol{u} = \boldsymbol{P} \cdot \nabla(\phi^{+} - \phi^{-}) = \boldsymbol{P} \cdot \nabla \Gamma \tag{2.3}$$

where $\boldsymbol{P} = \boldsymbol{I} - \boldsymbol{n}\boldsymbol{n}$ is the tangential projection operator, $\boldsymbol{I}$ is the identity matrix, ϕ^{+} and ϕ^{-} are the harmonic potentials evaluated on either side of the vortex sheet, and $\Gamma \equiv \phi^{+} - \phi^{-}$. It can be shown by standard arguments that Γ is the circulation along a closed loop that pierces the vortex sheet at a reference point and an arbitrary point, where the integral defining the circulation is directed as shown in figure 1.

The vectorial strength of the vortex sheet $\boldsymbol{\zeta}$ is related to the velocity discontinuity by the relation

$$\Delta \boldsymbol{u} \equiv \boldsymbol{\zeta} \times \boldsymbol{n}. \tag{2.4}$$

Taking the cross-product of both sides of equation (2.4) and the normal vector, noting that $\boldsymbol{\zeta}$ is tangential to the vortex sheet, and using (2.3), we find

$$\boldsymbol{\zeta} = \boldsymbol{n} \times \Delta \boldsymbol{u} = \boldsymbol{n} \times \nabla \Gamma. \tag{2.5}$$

In the case of two-dimensional flow, $\boldsymbol{\zeta}$ is taken to be parallel to the z-axis, whereupon the fluid velocity vector and jump $\Delta \boldsymbol{u}$ lie in the (x, y)-plane. In the case of axisymmetric flow, $\boldsymbol{\zeta}$ points in the direction of the meridional angle φ, and the fluid velocity and jump $\Delta \boldsymbol{u}$ lie in meridional planes over which φ is constant.

In terms of the strength of the vortex sheet, the velocity induced by the vortex sheet at the point $\boldsymbol{x}_0$ is given by the Biot-Savart integral

$$\boldsymbol{u}^{VS} = -\int_{D} \nabla G(\boldsymbol{x}, \boldsymbol{x}_0) \times \boldsymbol{\zeta}(\boldsymbol{x}) \, \mathrm{d}S(\boldsymbol{x}) \tag{2.6}$$

where the gradient ∇ operates with respect to the coordinates of the integration point $\boldsymbol{x}$, and D is an appropriate domain of integration, as will be discussed in the next paragraph. The scalar kernel $G(\boldsymbol{x}, \boldsymbol{x}_0)$ is a Neumann function of Laplace's equation corresponding to the periodicity of the flow, and observing the geometry of the boundaries. In the case of flow in an infinite domain and in the absence of boundaries, $G(\boldsymbol{x}, \boldsymbol{x}_0)$ is the free-space Green's function. More generally, $G(\boldsymbol{x}, \boldsymbol{x}_0)$ is chosen so that the Biot-Savart integral satisfies the no-penetration boundary condition, as required.

In the case of non-periodic flow, the integration domain D in (2.6) is the surface of the vortex sheet; for flow in free space, $G(\boldsymbol{x}, \boldsymbol{x}_0)$ represents the harmonic potential at the point $\boldsymbol{x}$ due to a point sink of unit strength located at the point $\boldsymbol{x}_0$, given by $G(\boldsymbol{x}, \boldsymbol{x}_0) = 1/(4\pi|\boldsymbol{x} - \boldsymbol{x}_0|)$. In the case of singly periodic flow, D is the portion of the vortex sheet enclosed by one period of the flow; for flow in free space, $G(\boldsymbol{x}, \boldsymbol{x}_0)$ represents the flow due to a one-dimensional array of point sinks of unit strength, one of which is located at the point $\boldsymbol{x}_0$. The computation of the singly periodic free-space

Green's function is discussed by Brady *et al.* (1998). In the case of doubly periodic flow, D is the portion of the vortex sheet enclosed by one period of the flow; for flow in free space, $G(\boldsymbol{x}, \boldsymbol{x}_0)$ represents the flow due to a doubly periodic array of point sinks of unit strength, one of which is located at the point $\boldsymbol{x}_0$. The computation of the doubly periodic free-space Green's function in terms of Ewald sums is discussed in Appendix A.

The principal velocity of the vortex sheet, denoted by $\boldsymbol{u}^{PV}$, is defined as the average of the fluid velocity on either side of the vortex sheet, and is given by

$$\boldsymbol{u}^{PV}(\boldsymbol{x}_0) \equiv \frac{\boldsymbol{u}^+(\boldsymbol{x}_0) + \boldsymbol{u}^-(\boldsymbol{x}_0)}{2} = \boldsymbol{u}^\infty(\boldsymbol{x}_0) - \int_D^{PV} \nabla G(\boldsymbol{x}, \boldsymbol{x}_0) \times \boldsymbol{\zeta}(\boldsymbol{x})\, \mathrm{d}S(\boldsymbol{x}) \tag{2.7}$$

where the point $\boldsymbol{x}_0$ lies on the vortex sheet. The principal value of the Biot-Savart integral may be regarded either as the limit of the non-singular integral that arises by excluding from the domain of integration a discoidal surface patch centred at the singular point, and then taking the limit as the size of the patch tends to zero, or as the average of the limiting values of the Biot-Savart integral that arises as the velocity point approaches the vortex sheet from either side. Expressing the variables of integration in local Cartesian coordinates with two axes tangential to the vortex sheet at a point, and examining the behaviour of the integrand with reference to standard integrals, we find that the two values are identical, as stated by Agishtein & Migdal (1989) and rigorously proved by Caflisch (1988) and Caflisch & Li (1992).

In terms of the principal velocity, the fluid velocity on either side of the vortex sheet is given by

$$\boldsymbol{u}^{\pm}(\boldsymbol{x}_0) = \boldsymbol{u}^{PV}(\boldsymbol{x}_0) \pm \tfrac{1}{2}\Delta\boldsymbol{u}(\boldsymbol{x}_0) = \boldsymbol{u}^{PV}(\boldsymbol{x}_0) \pm \tfrac{1}{2}\boldsymbol{\zeta}(\boldsymbol{x}_0) \times \boldsymbol{n}(\boldsymbol{x}_0) \tag{2.8}$$

which is the counterpart of the Plemelj formula in three dimensions.

The solenoidal vector potential of the flow induced by the vortex, denoted by $\boldsymbol{A}^{VS}$, is defined by the decomposition $\boldsymbol{u} = \boldsymbol{u}^\infty + \nabla \times \boldsymbol{A}^{VS}$ and is given by the integral representation

$$\boldsymbol{A}^{VS}(\boldsymbol{x}_0) = \int_D G(\boldsymbol{x}, \boldsymbol{x}_0) \times \boldsymbol{\zeta}(\boldsymbol{x})\, \mathrm{d}S(\boldsymbol{x}). \tag{2.9}$$

The flow due to a vortex sheet may be regarded as being induced by a double-layer potential whose scalar strength q is related to the strength of the vortex sheet by the equation

$$\boldsymbol{\zeta} = \boldsymbol{n} \times \nabla q \tag{2.10}$$

(e.g. Pozrikidis 1997, p. 502). Comparing (2.5) and (2.10) we find that, in fact, $q = \Gamma$. Substituting (2.10) into (2.9), and integrating by parts, we find an alternative expression for the vector potential in the terms of the circulation field,

$$\boldsymbol{A}^{VS}(\boldsymbol{x}_0) = -\int_D \Gamma(\boldsymbol{x})\, \boldsymbol{n}(\boldsymbol{x}) \times \nabla G(\boldsymbol{x}, \boldsymbol{x}_0)\, \mathrm{d}S(\boldsymbol{x}). \tag{2.11}$$

The kernel of the integral representation (2.11) has a strong singularity compared to that of (2.9).

In terms of the circulation, the harmonic potential at a point $\boldsymbol{x}_0$ that lies within either fluid is given by

$$\phi^{VS}(\boldsymbol{x}_0) = \int_D \Gamma(\boldsymbol{x})\, \boldsymbol{n}(\boldsymbol{x}) \cdot \nabla G(\boldsymbol{x}, \boldsymbol{x}_0)\, \mathrm{d}S(\boldsymbol{x}). \tag{2.12}$$

The properties of the Green's function ensure that shifting the level of the circulation generates a constant potential on either side of the vortex sheet with no consequence for the flow. The principal value of the harmonic potential is defined as the average of the two values of the potential on either side of the vortex sheet, and is equal to the principal value of the double-layer integral on the right-hand side of (2.12).

To describe the motion of a vortex sheet, we introduce a system of two surface curvilinear coordinates (ξ, η) defined over the evolving vortex sheet such that a tangential line of constant η, a tangential line of constant ξ, and a line that is parallel to the normal vector at a point comprise a system of right-handed local three-dimensional curvilinear coordinates, as shown in figure 1. Using (2.5) we find that, in terms of the circulation, the strength of the vortex sheet is given by

$$\boldsymbol{\zeta} = \frac{h_\xi h_\eta}{h_S}\left(\frac{\partial \Gamma}{\partial l_\xi}\,\boldsymbol{t}_\eta - \frac{\partial \Gamma}{\partial l_\eta}\,\boldsymbol{t}_\xi\right) \tag{2.13}$$

where h_ξ and h_η are metric coefficients for the arclength corresponding to ξ or η, l_ξ, l_η, are the corresponding arclengths, h_S is the metric coefficient for the surface area, and $\boldsymbol{t}_\xi$, $\boldsymbol{t}_\eta$ are unit vectors in the directions of the curvilinear axes corresponding to the respective subscript (Caflisch 1988; Agishtein & Migdal 1989; Kaneda 1990).

To this end, we regard the vortex sheet as a material surface consisting of a continuous distribution of marker points that are labelled permanently by the initial values of the curvilinear coordinates. Kinematic considerations require that the normal component of the marker point velocity be equal to the normal component of the velocity of the fluid on either side of the vortex sheet. The tangential component, however, may be arbitrary. In general, the marker point velocity, denoted by $\boldsymbol{U}$, may be assigned the form

$$\boldsymbol{U} = \boldsymbol{u}^{PV} + \boldsymbol{v} \tag{2.14}$$

where $\boldsymbol{v}$ is an arbitrary tangential vector field. When $\boldsymbol{v} = \boldsymbol{0}$, the marker points move with the principal velocity of the vortex sheet; whereas when $\boldsymbol{v} = -\boldsymbol{P} \cdot \boldsymbol{u}^{PV}$, the marker points move only normally to the vortex sheet. The appropriate choice of the marker point velocity depends on the character of the motion, and should be exercised with the practical objective of preventing marker point clustering leading to numerical instabilities and deterring the spatial resolution. For example, when the vortex sheet is stationary, it is appropriate to choose when $\boldsymbol{v} = -\boldsymbol{P} \cdot \boldsymbol{u}^{PV}$, so that the marker points are also stationary. When, on the other hand, the vortex translates as a rigid body with velocity $\boldsymbol{U}^{TR}$ without deformation, it is appropriate to choose $\boldsymbol{v} = \boldsymbol{P} \cdot (\boldsymbol{U}^{TR} - \boldsymbol{u}^{PV})$, so that the marker points retain their relative position.

The choice $\boldsymbol{v} = \boldsymbol{0}$ may be generalized by setting $\boldsymbol{v} = (\alpha - \frac{1}{2})\Delta \boldsymbol{u}$, where α is an arbitrary parameter. Substituting this expression into (2.14) we obtain the marker point velocity, a weighted average of the fluid velocity on either side of the vortex sheet,

$$\boldsymbol{U} = \alpha\, \boldsymbol{u}^{+} + (1 - \alpha)\, \boldsymbol{u}^{-}. \tag{2.15}$$

When $\alpha = 0$, $1/2$, 1, the marker points move, respectively, with the velocity of the fluid on the interior or lower side of the vortex sheet, the principal velocity of the vortex sheet, and the velocity of the fluid on the exterior or upper side of the vortex sheet. Although α may be assigned arbitrarily over the vortex sheet, for simplicity it will be assumed to be and remain constant and uniform over the vortex sheet during the motion.

The rate of change of a scalar or vectorial quantity q defined over the vortex sheet following the marker points is denoted as $\mathrm{d}/\mathrm{d}t$ and is given by

$$\frac{\mathrm{d}q}{\mathrm{d}t} \equiv \left(\frac{\partial q}{\partial t}\right)_{\xi,\eta} = \left(\frac{\partial q}{\partial t}\right)_{\boldsymbol{x}} + \boldsymbol{U}\cdot\nabla q \tag{2.16}$$

where the Eulerian derivatives on the right-hand side are computed after the function q has been extended into the whole space in an appropriate fashion.

If the position of the marker points is described by the function $\boldsymbol{X}(\xi,\eta,t)$, then the motion of the marker points is governed by the equation defining the marker point velocity,

$$\frac{\mathrm{d}\boldsymbol{X}}{\mathrm{d}t} = \boldsymbol{U} \tag{2.17}$$

subject to a specified initial condition. In addition to (2.17), we require an evolution equation for the jump in the velocity across the vortex sheet $\Delta\boldsymbol{u}$, the strength of the vortex sheet $\boldsymbol{\zeta}$, or the circulation Γ following the marker points. The derivation of these equations is now considered.

3. Vorticity dynamics

One way to derive an evolution equation for $\Delta\boldsymbol{u}$ or $\boldsymbol{\zeta}$ is to write Euler's equation for the motion of the fluid on either side of the vortex sheet, and then use (2.8) and (2.14) to express the velocities on either side of the vortex sheet in terms of (*a*) the principal velocity $\boldsymbol{u}^{PV}$ or marker point velocity $\boldsymbol{U}$, and (*b*) the jump in the velocity across the vortex sheet, $\Delta\boldsymbol{u}$. An alternative is discussed by Baker & Moore (1989). Working either way, we find that the rate of change of the velocity jump across the vortex sheet satisfies the equation

$$\frac{\mathrm{d}\Delta\boldsymbol{u}}{\mathrm{d}t} = -\Delta\boldsymbol{u}\cdot\nabla\boldsymbol{u}^{PV} + \boldsymbol{v}\cdot\nabla\Delta\boldsymbol{u} + 2A\left(\frac{\mathrm{d}\boldsymbol{u}^{PV}}{\mathrm{d}t} - \boldsymbol{v}\cdot\nabla\boldsymbol{u}^{PV} + \tfrac{1}{4}\Delta\boldsymbol{u}\cdot\nabla\Delta\boldsymbol{u}\right) + \frac{2}{\rho^{+}+\rho^{-}}\nabla(p^{-}-p^{+}) - 2A\,\boldsymbol{g} \tag{3.1}$$

where $\boldsymbol{v}$ is the tangential component of the marker point velocity defined in equation (2.14), $A = (\rho^{-}-\rho^{+})/(\rho^{-}+\rho^{+})$ is the Atwood ratio, and $\boldsymbol{g}$ is the acceleration due to gravity. To eliminate the pressures, we project equation (3.1) onto the tangential plane to form the tangential derivatives of the pressure, and then use the dynamic condition (2.1). To derive an evolution equation for $\boldsymbol{\zeta}$, we take the cross × product of (3.1) with the normal vector $\boldsymbol{n}$, and use the identity

$$\boldsymbol{n}\times\frac{\mathrm{d}\Delta\boldsymbol{u}}{\mathrm{d}t} = \frac{\mathrm{d}\boldsymbol{\zeta}}{\mathrm{d}t} + \boldsymbol{n}\left(\boldsymbol{\zeta}\cdot\frac{\mathrm{d}\boldsymbol{n}}{\mathrm{d}t}\right) \tag{3.2}$$

to extract the rate of change of $\boldsymbol{\zeta}$. The rate of change of the normal vector is given by

$$\frac{\mathrm{d}\boldsymbol{n}}{\mathrm{d}t} = -(\boldsymbol{P}\cdot\nabla\boldsymbol{U})\cdot\boldsymbol{n}. \tag{3.3}$$

When the flow on either side of the vortex sheet is irrotational, an evolution equation for the circulation Γ may be derived by considering Bernoulli's equation for the motion of the fluid on either side of the vortex sheet, as explained by Baker *et al.* (1982) and Baker (1983) for two-dimensional flow. Invoking the definition $\Gamma = \phi^{+} - \phi^{-}$, and expressing the velocity on either side of the vortex sheet in terms of the right-hand side of (2.8), we find

$$\frac{\mathrm{d}\Gamma}{\mathrm{d}t} = \boldsymbol{v} \cdot \Delta \boldsymbol{u} + 2A \left[\frac{\mathrm{d}\phi^{PV}}{\mathrm{d}t} - \tfrac{1}{2}(\boldsymbol{U} + \boldsymbol{v}) \cdot \boldsymbol{u}^{PV} + \tfrac{1}{8}|\Delta \boldsymbol{u}|^2 - \boldsymbol{g} \cdot \boldsymbol{x} \right] + \frac{2T}{\rho^+ + \rho^-}\, 2\kappa_m. \tag{3.4}$$

3.1. *Motion with a weighted average velocity*

When the marker point velocity is given by (2.15), the evolution equation for $\Delta \boldsymbol{u}$ takes the specific form

$$\begin{aligned} \frac{\mathrm{d}\Delta \boldsymbol{u}}{\mathrm{d}t} = -\boldsymbol{n} \left(\Delta \boldsymbol{u} \cdot \frac{\mathrm{d}\boldsymbol{n}}{\mathrm{d}t} \right) + 2\boldsymbol{P} \cdot \Bigg[& A\, \frac{\mathrm{d}\boldsymbol{u}^{PV}}{\mathrm{d}t} - A_3\, \Delta \boldsymbol{u} \cdot \nabla \boldsymbol{U} \\ & + A_4\, \Delta \boldsymbol{u} \cdot \nabla \Delta \boldsymbol{u} + \frac{2T}{\rho^+ + \rho^-}\, \nabla \kappa_m - A\, \boldsymbol{g} \Bigg] \end{aligned} \tag{3.5}$$

where

$$A_3 = \frac{\rho^+ + \alpha(\rho^- - \rho^+)}{\rho^- + \rho^+}, \qquad A_4 = \frac{\rho^- \alpha^2 - \rho^+(1-\alpha)^2}{\rho^- + \rho^+}. \tag{3.6}$$

The first term on the right-hand side of (3.5) expresses the component of $\mathrm{d}\Delta \boldsymbol{u}/\mathrm{d}t$ normal to the vortex sheet. The rest of the terms on the right-hand side express the component of $\mathrm{d}\Delta \boldsymbol{u}/\mathrm{d}t$ tangential to the vortex sheet. The rate of change of the principal velocity of the vortex sheet in the second term on the right-hand side of (3.5) is found by differentiating (2.7), obtaining

$$\begin{aligned} \left(\frac{\mathrm{d}\boldsymbol{u}^{PV}(\boldsymbol{x}_0)}{\mathrm{d}t} \right)_{t=t_0} = \left(\frac{\mathrm{d}\boldsymbol{u}^{\infty}(\boldsymbol{x}_0)}{\mathrm{d}t} \right)_{t=t_0} & - \int_D^{PV} \nabla G(\boldsymbol{x}, \boldsymbol{x}_0) \times \left(\frac{\mathrm{d}\boldsymbol{\zeta}(\boldsymbol{x})}{\mathrm{d}t} \right)_{t=t_0} \mathrm{d}S(\boldsymbol{x}) \\ & - \frac{\mathrm{d}}{\mathrm{d}t} \int_D^{PV} \nabla G(\boldsymbol{x}, \boldsymbol{x}_0) \times \boldsymbol{\zeta}(\boldsymbol{x}, t_0)\, \mathrm{d}S(\boldsymbol{x}). \end{aligned} \tag{3.7}$$

Expressing $\boldsymbol{\zeta}$ in terms of $\Delta \boldsymbol{u}$ using (2.5), and substituting the result into (3.7) and the outcome into (3.5), we obtain a Fredholm integral equation of the second kind for $\mathrm{d}\Delta \boldsymbol{u}/\mathrm{d}t$ that may be stated in the symbolic form

$$\begin{aligned} & \frac{\mathrm{d}\Delta \boldsymbol{u}}{\mathrm{d}t}(\boldsymbol{x}_0, t_0) \\ & \quad = -2A \int_D^{PV} \boldsymbol{P}(\boldsymbol{x}_0) \cdot \left\{ \nabla G(\boldsymbol{x}, \boldsymbol{x}_0) \times \left[\boldsymbol{n}(\boldsymbol{x}) \times \left(\frac{\mathrm{d}\Delta \boldsymbol{u}(\boldsymbol{x})}{\mathrm{d}t} \right)_{t=t_0} \right] \right\} \mathrm{d}S(\boldsymbol{x}) + \boldsymbol{J}(x_0, t_0) \end{aligned} \tag{3.8}$$

where $\boldsymbol{J}$ is a forcing function. To this end, we note that the normal component of $\mathrm{d}\Delta \boldsymbol{u}/\mathrm{d}t$ is given explicitly by the first term on the right-hand side of (3.5) which has been absorbed into the forcing function $\boldsymbol{J}$; thus, (3.8) is truly an integral equation for the tangential component of $\mathrm{d}\Delta \boldsymbol{u}/\mathrm{d}t$. As the integration point $\boldsymbol{x}$ approaches the field point $\boldsymbol{x}_0$, the gradient of the Green's function on the right-hand side of (3.8) tends to become tangential to the vortex sheet, exhibiting a $1/r^2$ singularity that matches the dimension of the domain of integration, where $r = |\boldsymbol{x} - \boldsymbol{x}_0|$. It appears then that the integral operator is not compact even when the normal vector is continuous over the vortex sheet. We note, however, that as $\boldsymbol{x}$ approaches $\boldsymbol{x}_0$, the integrand in (3.8) behaves as

$$\frac{1}{r^2} \boldsymbol{P}(\boldsymbol{x}_0) \cdot \left\{ \frac{\boldsymbol{x} - \boldsymbol{x}_0}{r} \times \left[\boldsymbol{n}(\boldsymbol{x}) \times \left(\frac{\mathrm{d}\Delta \boldsymbol{u}(\boldsymbol{x})}{\mathrm{d}t} \right)_{t=t_0} \right] \right\}. \tag{3.9}$$

The cross-product of the two terms within the square brackets tends to become tangential to the vortex sheet, and the cross-product of the two terms within the curly brackets tends to become perpendicular to the vortex sheet and its projection onto the tangential plane tends to vanish at a linear rate with respect to r. Consequently, the singularity is truly on the order of $1/r$, and the integral operator in (3.9) is only weakly singular.

The compactness of the integral operator allows us to study the properties of the integral equation and assess the convergence of Neumann iterations working within the framework of the Riesz–Fredholm theory, as discussed by Baker *et al.* (1982) for two-dimensional flow. This result is consistent with the aforementioned equivalence of the flow due to a vortex sheet and the flow due to a double-layer potential whose density is equal to the circulation field. The spectral analysis of the double-layer potential operator reveals that the integral equation (3.8) has a globally convergent Neumann series, and the solution can be found using the method of successive substitutions provided that the magnitude Atwood ratio is not equal to unity; that is, provided that the density of neither fluid is equal to zero.

The evolution equation for the strength of the vortex sheet corresponding to equation (3.5) is found to be

$$\frac{\mathrm{d}\boldsymbol{\zeta}}{\mathrm{d}t} = -\boldsymbol{n}\left(\boldsymbol{\zeta}\cdot\frac{\mathrm{d}\boldsymbol{n}}{\mathrm{d}t}\right) + 2\boldsymbol{n}\times\left[A\,\frac{\mathrm{d}\boldsymbol{u}^{PV}}{\mathrm{d}t} - A_3\,\Delta\boldsymbol{u}\cdot\nabla\boldsymbol{U} + A_4\,\Delta\boldsymbol{u}\cdot\nabla\Delta\boldsymbol{u} + \frac{2T}{\rho^+ + \rho^-}\,\nabla\kappa_m - A\,\boldsymbol{g}\right]. \qquad (3.10)$$

Repeating the preceding arguments, we find that (3.10) is a Fredholm integral equation of the second kind for the tangential component of $\mathrm{d}\boldsymbol{\zeta}/\mathrm{d}t$ whose properties are similar to those of (3.8) discussed in the preceding paragraph.

The associated evolution equation for the circulation is found to be

$$\frac{\mathrm{d}\Gamma}{\mathrm{d}t} = (\alpha - \tfrac{1}{2})\,|\Delta\boldsymbol{u}|^2 + 2A\left\{\frac{\mathrm{d}\phi^{PV}}{\mathrm{d}t} - \tfrac{1}{2}\left[\boldsymbol{u}^{PV} + (2\alpha - 1)\,\Delta\boldsymbol{u}\right]\cdot\boldsymbol{u}^{PV} + \tfrac{1}{8}|\Delta\boldsymbol{u}|^2 - \boldsymbol{g}\cdot\boldsymbol{x}\right\} + \frac{2T}{\rho^+ + \rho^-}\,2\,\kappa_m \qquad (3.11)$$

which is a Fredholm integral equation of the second kind for $\mathrm{d}\Gamma/\mathrm{d}t$. Differentiating (2.3) in time following the marker points, using (3.11), and carrying out a fair amount of algebra, we recover (3.8).

3.2. *Motion with the principal velocity*

When the marker points move with the principal velocity of the vortex sheet, corresponding to $\alpha = \frac{1}{2}$, in which case $A_3 = \frac{1}{2}$ and $A_4 = \frac{1}{4}A$, the evolution equations (3.8) and (3.10) simplify to

$$\frac{\mathrm{d}\Delta\boldsymbol{u}}{\mathrm{d}t} = \Delta\boldsymbol{u}\cdot(\nabla\boldsymbol{u}^{PV})\cdot(\boldsymbol{I} - 2\boldsymbol{P}) + 2A\,\boldsymbol{P}\cdot(\bar{\boldsymbol{a}} - \boldsymbol{g}) + \frac{4T}{\rho^+ + \rho^-}\,\boldsymbol{P}\cdot\nabla\kappa_m, \qquad (3.12)$$

$$\frac{\mathrm{d}\boldsymbol{\zeta}}{\mathrm{d}t} = \boldsymbol{n}[\boldsymbol{\zeta}\cdot(\nabla\boldsymbol{u}^{PV})\cdot\boldsymbol{n}] - \boldsymbol{n}\times(\Delta\boldsymbol{u}\cdot\nabla\boldsymbol{u}^{PV}) + 2A\,\boldsymbol{n}\times(\bar{\boldsymbol{a}} - \boldsymbol{g}) + \frac{4T}{\rho^+ + \rho^-}\,\boldsymbol{n}\times\nabla\kappa_m \qquad (3.13)$$

where

$$\bar{\boldsymbol{a}} = \frac{1}{2}\left(\frac{\mathrm{D}\boldsymbol{u}^+}{\mathrm{D}t} + \frac{\mathrm{D}\boldsymbol{u}^-}{\mathrm{D}t}\right) = \frac{\mathrm{d}\boldsymbol{u}^{PV}}{\mathrm{d}t} + \tfrac{1}{4}\Delta\boldsymbol{u}\cdot\nabla\Delta\boldsymbol{u} \tag{3.14}$$

is the average acceleration of the fluid on either side of the vortex sheet, and $\mathrm{D}/\mathrm{D}t$ is the material derivative. Correspondingly, the evolution equation (3.11) simplifies to

$$\frac{\mathrm{d}\Gamma}{\mathrm{d}t} = 2A\left(\frac{\mathrm{d}\phi^{PV}}{\mathrm{d}t} - \tfrac{1}{2}|\boldsymbol{u}^{PV}|^2 + \tfrac{1}{8}|\Delta\boldsymbol{u}|^2 - \boldsymbol{g}\cdot\boldsymbol{x}\right) + \frac{2T}{\rho^+ + \rho^-}\,2\kappa_m. \tag{3.15}$$

When the flow on either side of the vortex sheet is irrotational, we write $\boldsymbol{n}\cdot(\nabla\times\boldsymbol{u}^{PV}) = 0$, and find that the first two terms on the right-hand side of (3.13) combine to yield the alternative form

$$\frac{\mathrm{d}\boldsymbol{\zeta}}{\mathrm{d}t} = \boldsymbol{\zeta}\cdot(\nabla\boldsymbol{u}^{PV}) - \boldsymbol{\zeta}\,(\boldsymbol{P}\cdot\nabla\cdot\boldsymbol{u}^{PV}) + 2A\,\boldsymbol{n}\times(\bar{\boldsymbol{a}} - \boldsymbol{g}) + \frac{4T}{\rho^+ + \rho^-}\,\boldsymbol{n}\times\nabla\kappa_m \tag{3.16}$$

which is in agreement with equation (64) derived by Wu (1995) using a different approach. Furthermore, using an identity derived in Appendix B, we write

$$\frac{\mathrm{d}\Delta\boldsymbol{u}}{\mathrm{d}t} = \frac{\mathrm{d}}{\mathrm{d}t}(\boldsymbol{P}\cdot\nabla\Gamma) = \boldsymbol{P}\cdot\nabla\frac{\mathrm{d}\Gamma}{\mathrm{d}t} + \Delta\boldsymbol{u}\cdot(\nabla\boldsymbol{u}^{PV})\cdot(\boldsymbol{I} - 2\boldsymbol{P}) \tag{3.17}$$

and recast equation (3.12) in terms of the circulation over the vortex sheet in the form

$$\boldsymbol{P}\cdot\nabla\frac{\mathrm{d}\Gamma}{\mathrm{d}t} = 2A\,\boldsymbol{P}\cdot(\bar{\boldsymbol{a}} - \boldsymbol{g}) + \frac{4T}{\rho^+ + \rho^-}\,\boldsymbol{P}\cdot\nabla\kappa_m. \tag{3.18}$$

Invoking the definition of the mean acceleration defined in terms of the material derivative in equation (3.14), and using Bernoulli's equation for unsteady irrotational flow, we find

$$\bar{\boldsymbol{a}} = \nabla\left(\frac{\mathrm{d}\phi^{PV}}{\mathrm{d}t} - \tfrac{1}{2}|\boldsymbol{u}^{PV}|^2 + \tfrac{1}{8}|\Delta\boldsymbol{u}|^2\right). \tag{3.19}$$

Substituting this expression into the left-hand side of (3.18), and integrating over the vortex sheet, we recover equation (3.15) governing the evolution of the circulation.

When the densities of the fluids are matched, in which case the Atwood ratio vanishes, $A = 0$, we obtain a simple evolution law for the circulation

$$\frac{\mathrm{d}\Gamma}{\mathrm{d}t} = \frac{T}{\rho}\,2\kappa_m. \tag{3.20}$$

In the absence of surface tension, $T = 0$, we obtain a conservation law derived previously by Caflisch (1988), Agishtein & Migdal (1989), Kaneda (1990), and Caflisch & Li (1992) using direct methods. The stipulations leading to (3.20) with vanishing surface tension have been described as the 'Lagrangian formulation' by these authors.

When the marker point velocity is equal to the velocity of the fluid normal to the vortex sheet, we obtain a different set of evolution equations. When $A = 0$, corresponding to a vortex sheet immersed in a homogeneous fluid, the evolution equations for $\Delta\boldsymbol{u}$, $\boldsymbol{\zeta}$, and Γ are identical to (3.12), (3.13), and (3.15), except that the convective term $-\boldsymbol{P}\cdot\boldsymbol{u}^{PV}\cdot\nabla\Delta\boldsymbol{u}$, $-\boldsymbol{n}\times(\boldsymbol{u}^{PV}\cdot\nabla\Delta\boldsymbol{u})$, or $\boldsymbol{P}\cdot\boldsymbol{u}^{PV}\cdot\nabla\Gamma$, respectively, is also present on the right-hand side.

4. Computation of the self-induced velocity

To compute the motion of marker points moving with a weighted average of the fluid velocity on either side of the vortex sheet, we require the principal value of the Biot-Savart integral. To compute the motion of marker points moving normal to the vortex sheet, we require only the normal component of the Biot-Savart integral. Even in the second case, however, the tangential component is necessary for evaluating the rate of change of the strength of the vortex sheet or circulation following the marker points.

To compute the Biot-Savart integral, a closed vortex sheet, or one period of a singly or doubly periodic vortex sheet, is triangulated into a network of quadratic curved triangles defining six nodes: three vertex nodes and three mid-nodes. The position vector, circulation field, Cartesian components of the strength of the vortex sheet, and Cartesian components of the jump in velocity across the vortex sheet are approximated with quadratic basis function in terms of local triangle coordinates given, for example, in Pozrikidis (1998). With this type of discretization, the tangential derivatives of surface functions and the components of the normal vector undergo a discontinuity across the element edges. Whenever the normal vector or another discontinuous surface function is needed at the nodes, it is computed by averaging its components at the local nodes of all adjacent triangles. In the case of the normal vector, averaging is followed by normalization.

4.1. *Computation of the normal component of the velocity in terms of the vector potential*

Baker (1983) developed an indirect method of computing the component of the fluid velocity normal to the vortex sheet that involves three steps: (*a*) introduce the vector potential $\boldsymbol{A}^{VS}$ associated with the vortex sheet defined by the equation $\boldsymbol{u} = \boldsymbol{u}^{\infty} + \nabla \times \boldsymbol{A}^{VS}$; (*b*) evaluate the vector potential over the vortex sheet using the integral representation (2.9) or (2.11); and (*c*) differentiate the components of the vector potential in the tangential plane to obtain the normal component of the velocity induced by the vortex sheet.

In the present implementation, the surface integral (2.9) is computed by integrating over the collection of the curved triangles distributed over the vortex sheet. As the integration point $\boldsymbol{x}$ approaches the evaluation point $\boldsymbol{x}_0$, the kernel of the vector-potential integral operator on the right-hand side of (2.9) exhibits a weak singularity, diverging as $1/|\boldsymbol{x} - \boldsymbol{x}_0|$. The integral over a singular triangle that contains the point evaluation point $\boldsymbol{x}_0$ as a node is computed by integrating in local triangle polar coordinates centred at the singular point, using the double Gauss–Legendre quadrature. Specifically, when $\boldsymbol{x}_0$ is a vertex node, the integral is computed over the flat triangle defined by the three vertex nodes, whereas when $\boldsymbol{x}_0$ is a mid-node, the integral is computed over four flat triangles defined by the mid-node and pairs of the rest of the vertex and mid-nodes. The integral over the non-singular triangles is computed using a triangle quadrature (e.g. Pozrikidis 1998).

As an alternative, the vector potential may be evaluated from the integral representation (2.11). As the integration point $\boldsymbol{x}$ approaches the field point $\boldsymbol{x}_0$, the gradient of the Green's function tends to become tangential to the vortex sheet, exhibiting a $1/|\boldsymbol{x} - \boldsymbol{x}_0|^2$ singularity. Baker (1983) noted that the identity

$$\int_D \boldsymbol{n}(\boldsymbol{x}) \times \nabla G(\boldsymbol{x}, \boldsymbol{x}_0)\, \mathrm{d}S(\boldsymbol{x}) = 0 \tag{4.1}$$

allows us to subtract off the singularity by writing

$$A^{VS}(\boldsymbol{x}_0) = -\int_D [\Gamma(\boldsymbol{x}) - \Gamma(\boldsymbol{x}_0)]\ \boldsymbol{n}(x) \times \nabla G(\boldsymbol{x}, \boldsymbol{x}_0)\, \mathrm{d}S(\boldsymbol{x}). \tag{4.2}$$

The integrand on the right-hand side of (4.2) diverges only weakly as $1/|\boldsymbol{x} - \boldsymbol{x}_0|$, and the integral may be computed using the numerical method described in the last paragraph.

Once the vector potential is available at all marker points, the three columns of the Frechet derivative $\nabla \boldsymbol{A}^{VS}$ are computed at the nodes of the triangles by solving the following three systems of three linear equations:

$$\frac{\partial \boldsymbol{x}}{\partial \xi} \cdot \nabla \boldsymbol{A}^{VS} = \frac{\partial \boldsymbol{A}^{VS}}{\partial \xi}, \qquad \frac{\partial \boldsymbol{x}}{\partial \eta} \cdot \nabla \boldsymbol{A}^{VS} = \frac{\partial \boldsymbol{A}^{VS}}{\partial \eta}, \qquad \boldsymbol{n} \cdot \nabla \boldsymbol{A}^{VS} = \boldsymbol{0}. \tag{4.3}$$

where ξ and η are local triangle coordinates, and $\boldsymbol{n}$ is the normal vector at the nodes averaged over the host elements. Computing the tangential derivatives of $\boldsymbol{A}^{VS}$ in this fashion is simpler and more expedient than taking derivatives with respect to the surface curvilinear coordinates. Following this computation, the matrix $\nabla \boldsymbol{A}^{VS}$ is averaged at the nodes over the neighbouring elements, and the curl $\nabla \times \boldsymbol{A}^{VS}$ arises from its skew-symmetric component. Finally, projecting $\nabla \times \boldsymbol{A}^{VS}$ in the direction normal to the vortex sheet yields the normal component of the velocity.

To test the accuracy of the method, we consider uniform flow with velocity U along the x-axis past a stationary sphere of radius a centred at the origin, and represent the velocity field by a superposition of the incident streaming flow and the flow induced by a vortex sheet with strength $\boldsymbol{\zeta} = -\frac{3}{2} U a\, \boldsymbol{e}_\varphi$, where $\boldsymbol{e}_\varphi$ is the unit vector pointing in the meridional direction around the x-axis. The level of triangulation is determined by the index N_{tr}; when $N_{tr} = 0$, the vortex sheet is divided into eight curved triangles that arise by projecting the vertices and mid-points of the edges of an octahedron onto the sphere; when $N_{tr} = 1$, each triangle is subdivided into four descendant triangles generated by connecting the vertex and mid-point nodes; each time N_{tr} is increased by one unit, a further subdivision is carried out, quadrupling the number of elements. The RMS value of the relative error in the normal component of the marker point velocity for $N_{tr} = 0$, 1, 2, 3, corresponding to 8, 32, 128, and 512 elements, is found to be, respectively, 0.015840, 0.00288, 0.000244, and 0.00002395, which suggests that the results converge linearly with respect to the size of the boundary elements, as expected.

4.2. *Computation of the tangential component of the velocity in terms of the harmonic potential*

Baker (1983) developed an indirect method of computing the component of the fluid velocity tangential to a vortex sheet in terms of the circulation field; the latter is either provided or computed from the strength of the vortex sheet by surface integration. The numerical method involves evaluating the principal value of the harmonic potential over the vortex sheet using the integral representation (2.12), and then computing its tangential gradient.

As the integration point $\boldsymbol{x}$ approaches the evaluation point $\boldsymbol{x}_0$, the kernel of (2.12) exhibits a $1/|\boldsymbol{x} - \boldsymbol{x}_0|$ singularity. Use of the polar integration rule over flat triangles to annihilate this singularity is prohibited by the fact that the kernel of the integral representation vanishes identically over a flat surface passing through the singular point. Consequently, neglecting the curvature of the vortex sheet introduces an error on the order of the mean radius of curvature multiplied by the typical element size.

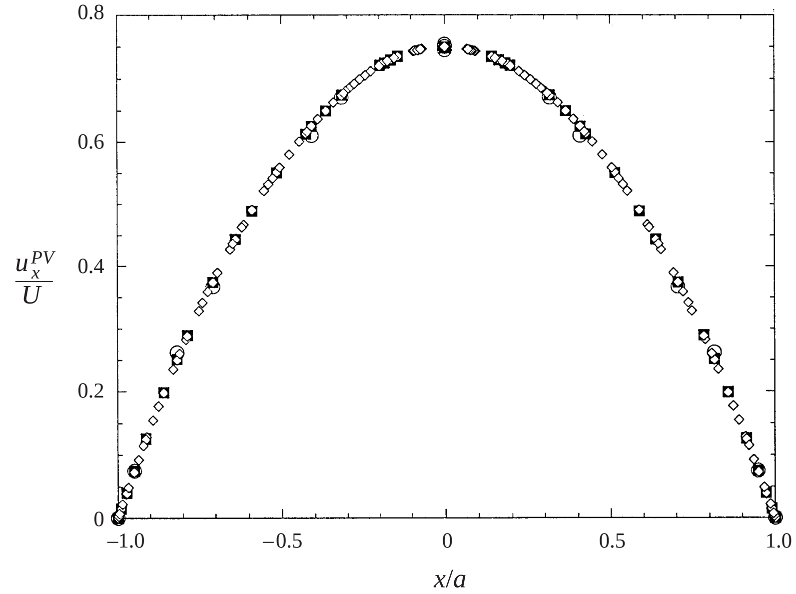

FIGURE 2. Test of accuracy in the evaluation of the tangential component of the velocity for streaming flow with velocity U along the x-axis past a stationary sphere of radius a. The tangential velocity is computed by taking tangential derivatives of the principal value of the harmonic potential. The figure shows a graph of the x-component of the principal velocity at the marker points for three levels of discretization. The circles, squares, and diamonds correspond, respectively, to discretization into 128, 256, and 512 elements. In the exact solution, the data fall on a sinusoidal curve with amplitude 0.75.

To circumvent this difficulty in the case of a closed vortex sheet, we use the identity

$$\int_D^{PV} \boldsymbol{n}(\boldsymbol{x}) \cdot \nabla G(\boldsymbol{x}, \boldsymbol{x}_0)\, \mathrm{d}S(\boldsymbol{x}) = -\tfrac{1}{2} \tag{4.4}$$

and write

$$\phi^{VS}(\boldsymbol{x}_0) = \int_D [\Gamma(\boldsymbol{x}) - \Gamma(\boldsymbol{x}_0)]\ \boldsymbol{n}(\boldsymbol{x}) \cdot \nabla G(\boldsymbol{x}, \boldsymbol{x}_0)\, \mathrm{d}S(\boldsymbol{x}) - \tfrac{1}{2}\Gamma(\boldsymbol{x}_0). \tag{4.5}$$

As the integration point $\boldsymbol{x}$ approaches the evaluation point $\boldsymbol{x}_0$, the kernel of the integral on the right-hand side of (4.5) tends to a finite value that depends on the direction of $\boldsymbol{x} - \boldsymbol{x}_0$. The integral is computed with sufficient accuracy over regular and singular triangles using a triangle quadrature. Once the principal value of the potential is available at all surface nodes, its tangential gradient is computed using the counterpart of equations (4.3).

To assess the accuracy of the method, we repeated the computations described at the end of §4.1 for uniform flow past a stationary sphere represented by a vortex sheet. Figure 2 displays the x-component of the principal velocity at the marker points for three levels of discretization. In the absence of numerical error, the data should fall on a sinusoidal curve with amplitude $0.75U$. For the third level of discretization corresponding to 512 boundary elements, the maximum relative error is on the order of 0.1%, which demonstrates the effectiveness of the numerical method even when a moderate number of boundary elements are employed.

4.3. *Direct computation of the Biot-Savart integral*

The direct computation of the principal value of the self-induced velocity of the vortex sheet, given in equation (2.6) where the point $\boldsymbol{x}_0$ lies on the vortex sheet, is more challenging. It was mentioned earlier that a central difficulty is that the principal value of the Biot-Savart integral exists only when the normal vector varies in a continuous fashion over the vortex sheet, that is, when the vortex sheet is a Lyapunov surface. If the normal vector is discontinuous at a point, then the principal value is not defined. This mathematical condition stems from the physical requirement of continuous vortex lines for a solenoidal vorticity field and a non-singular velocity field. The demand on smoothness appears to invalidate local vortex-sheet discretization into non-smooth approximated surfaces, including the discretization into quadratic triangles employed on the present study; the use of high-order global or local discretization defined in terms of Hermite interpolation appears imperative. Previous investigators circumvented this difficulty by regularizing the Biot-Savart kernel, thereby replacing the jump in the velocity across the vortex sheet with a rapidly varying distribution. We find that the demand on geometrical smoothness may be bypassed by subtracting off the Biot-Savart singularity and then using integral identities to account for its contribution, working as follows.

For illustration, we consider a closed vortex sheet, and recast the principal value of the self-induced velocity given in (2.7) in the form

$$\boldsymbol{u}^{PV}(\boldsymbol{x}_0) = \boldsymbol{u}^{\infty}(\boldsymbol{x}_0) - \int_D \nabla G(\boldsymbol{x}, \boldsymbol{x}_0) \times [\boldsymbol{\zeta}(\boldsymbol{x}) - \boldsymbol{\zeta}(\boldsymbol{x}_0)]\, \mathrm{d}S(\boldsymbol{x}) + \boldsymbol{\zeta}(\boldsymbol{x}_0) \times \int_D^{PV} \nabla G(\boldsymbol{x}, \boldsymbol{x}_0)\, \mathrm{d}S(\boldsymbol{x}). \tag{4.6}$$

As the integration point $\boldsymbol{x}$ approaches the evaluation point $\boldsymbol{x}_0$, the kernel of the first integral on the right-hand side of (4.6) diverges weakly as $1/|\boldsymbol{x}-\boldsymbol{x}_0|$, and the integral may be computed with sufficient accuracy using a numerical method that is analogous to that described in § 4.1 for the vector potential.

To compute the principal value of the last integral on the right-hand side of (4.6), we express it in the form

$$\int_D^{PV} \nabla G(\boldsymbol{x}, \boldsymbol{x}_0)\, \mathrm{d}S(\boldsymbol{x}) = \int_D^{PV} [\boldsymbol{n}(\boldsymbol{x}) - \boldsymbol{n}(\boldsymbol{x}_0)]\; \boldsymbol{n}(\boldsymbol{x}) \cdot \nabla G(\boldsymbol{x}, \boldsymbol{x}_0)\, \mathrm{d}S(\boldsymbol{x}) + \boldsymbol{n}(\boldsymbol{x}_0) \int_D^{PV} \boldsymbol{n}(\boldsymbol{x}) \cdot \nabla G(\boldsymbol{x}, \boldsymbol{x}_0)\, \mathrm{d}S(\boldsymbol{x}) + \int_D^{PV} \boldsymbol{P}(\boldsymbol{x}) \cdot \nabla G(\boldsymbol{x}, \boldsymbol{x}_0)\, \mathrm{d}S(\boldsymbol{x}) \tag{4.7}$$

where $\boldsymbol{P} = \boldsymbol{I} - \boldsymbol{nn}$ is the tangential projection operator. As the integration point $\boldsymbol{x}$ approaches the evaluation point $\boldsymbol{x}_0$, the kernel of the first integral on the right-hand side of (4.7) tends to a finite value that depends on the direction of $\boldsymbol{x}-\boldsymbol{x}_0$. This integral may be computed with sufficient accuracy using a triangle quadrature. Conservation of mass for the flow due to a point sink requires that the principal value of the second integral on the left-hand side of (4.7) is equal to $-\frac{1}{2}$.

To compute the last integral on the right-hand side of (4.7), we use Stokes's theorem of vector calculus and derive the identity

$$\oint_C \boldsymbol{F} \times \boldsymbol{t}\, \mathrm{d}l = \int_{\Omega} [\boldsymbol{n}\; \nabla \cdot \boldsymbol{F} - (\nabla \boldsymbol{F}) \cdot \boldsymbol{n}]\, \mathrm{d}S \tag{4.8}$$

where Ω is an arbitrary open surface bounded by the closed contour C, $\boldsymbol{n}$ is the unit vector normal to Ω, $\boldsymbol{t}$ is the unit vector tangential to C and Ω, and $\boldsymbol{F}$ is an arbitrary vector function defined over Ω (e.g. Pozrikidis 1997, p. 640). Selecting $\boldsymbol{F}(\boldsymbol{x}) = G(\boldsymbol{x}, \boldsymbol{x}_0)\, \boldsymbol{n}(\boldsymbol{x})$, and noting that, because the length of the unit normal vector is fixed, $(\nabla \boldsymbol{n}) \cdot \boldsymbol{n} = 0$, we find

$$\oint_C G(\boldsymbol{x}, \boldsymbol{x}_0)\; \boldsymbol{n} \times \boldsymbol{t}\, \mathrm{d}l = -\int_\Omega \boldsymbol{P}(\boldsymbol{x}) \cdot \nabla G(\boldsymbol{x}, \boldsymbol{x}_0)\, \mathrm{d}S + \int_\Omega 2\kappa_m(\boldsymbol{x})\; G(\boldsymbol{x}, \boldsymbol{x}_0)\; \boldsymbol{n}(\boldsymbol{x})\, \mathrm{d}S \qquad (4.9)$$

where $\kappa_m = \frac{1}{2}\nabla \cdot \boldsymbol{n}$ is the mean curvature; the vector $\boldsymbol{t} \times \boldsymbol{n}$ is tangential to the surface and lies in a plane that is normal to C. Identifying now Ω with the surface of a closed vortex sheet, denoted by D, excluding from it a small discoidal surface of radius ϵ centred at the singular point $\boldsymbol{x}_0$, and letting ϵ tend to zero, we find

$$\int_D^{PV} \boldsymbol{P}(\boldsymbol{x}) \cdot \nabla G(\boldsymbol{x}, \boldsymbol{x}_0)\, \mathrm{d}S = \int_D 2\kappa_m(\boldsymbol{x})\; G(\boldsymbol{x}, \boldsymbol{x}_0)\; \boldsymbol{n}(\boldsymbol{x})\, \mathrm{d}S. \qquad (4.10)$$

The kernel of the integral on the right-hand side of (4.10) diverges only weakly as $1/|\boldsymbol{x} - \boldsymbol{x}_0|$, and the integral may be computed accurately using a numerical method similar to that described earlier for the vector potential.

It is reassuring to observe that the Green's function in all preceding expressions may be enhanced by a constant, but the integral identity

$$\int_D 2\kappa_m(\boldsymbol{x})\; \boldsymbol{n}(\boldsymbol{x})\, \mathrm{d}S = 0 \qquad (4.11)$$

which arises by applying (4.8) with $\boldsymbol{F}(\boldsymbol{x}) = \boldsymbol{n}(\boldsymbol{x})$, guarantees that this modification will not affect the value of the integral on the right-hand side of (4.10). Thus, identity (4.10) is consistent with the expected independence of the flow on the base level of the vector or harmonic potential.

It is important to note that, if the surface D were discretized into flat elements, such as three-node triangles, the integral on the right-hand side of (4.10) would be identically equal to zero, and use of formula (4.10) would incur an error on the order of unity. For example, integrating over the surface of a sphere in spherical polar coordinates, we find

$$\int_{Sphere} 2\kappa_m(\boldsymbol{x})\; G(\boldsymbol{x}, \boldsymbol{x}_0)\; \boldsymbol{n}(\boldsymbol{x})\, \mathrm{d}S = \tfrac{2}{3}\boldsymbol{n}(\boldsymbol{x}_0). \qquad (4.12)$$

This result underscores the importance of maintaining the curvature of a vortex sheet in the surface element discretization.

Returning to (4.7), we combine the preceding results and write

$$\begin{aligned}\int_D^{PV} \nabla G(\boldsymbol{x}, \boldsymbol{x}_0)\, \mathrm{d}S(\boldsymbol{x}) = {} & \int_D^{PV} [\boldsymbol{n}(\boldsymbol{x}) - \boldsymbol{n}(\boldsymbol{x}_0)]\; \boldsymbol{n}(\boldsymbol{x}) \cdot \nabla G(\boldsymbol{x}, \boldsymbol{x}_0)\, \mathrm{d}S(\boldsymbol{x}) \\ & -\tfrac{1}{2}\; \boldsymbol{n}(\boldsymbol{x}_0) + \int_D 2\kappa_m(\boldsymbol{x})\; G(\boldsymbol{x}, \boldsymbol{x}_0)\; \boldsymbol{n}(\boldsymbol{x})\, \mathrm{d}S(\boldsymbol{x}). \qquad (4.13)\end{aligned}$$

Substituting this expression into (4.6), we obtain the final result for a closed vortex sheet

$$\begin{aligned}\boldsymbol{u}^{PV}(\boldsymbol{x}_0) = {} & \boldsymbol{u}^{\infty}(\boldsymbol{x}_0) - \tfrac{1}{2}\; \boldsymbol{\zeta}(\boldsymbol{x}_0) \times \boldsymbol{n}(\boldsymbol{x}_0) - \int_D \nabla G(\boldsymbol{x}, \boldsymbol{x}_0) \times [\boldsymbol{\zeta}(\boldsymbol{x}) - \boldsymbol{\zeta}(\boldsymbol{x}_0)]\, \mathrm{d}S(\boldsymbol{x}) \\ & + \boldsymbol{\zeta}(\boldsymbol{x}_0) \times \int_D^{PV} [\boldsymbol{n}(\boldsymbol{x}) - \boldsymbol{n}(\boldsymbol{x}_0)]\; \boldsymbol{n}(\boldsymbol{x}) \cdot \nabla G(\boldsymbol{x}, \boldsymbol{x}_0)\, \mathrm{d}S(\boldsymbol{x}) \\ & + \boldsymbol{\zeta}(\boldsymbol{x}_0) \times \int_D 2\kappa_m(\boldsymbol{x})\; G(\boldsymbol{x}, \boldsymbol{x}_0)\; \boldsymbol{n}(\boldsymbol{x})\, \mathrm{d}S(\boldsymbol{x}). \qquad (4.14)\end{aligned}$$

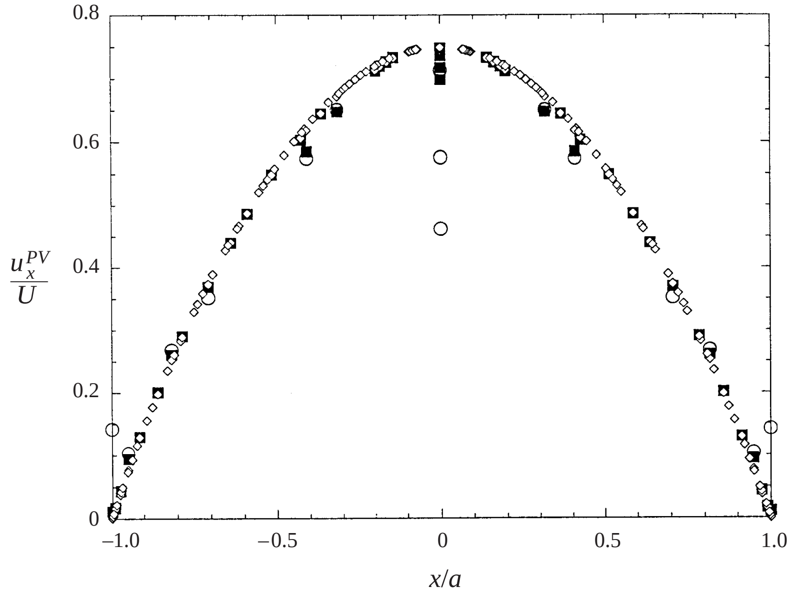

FIGURE 3. Same as figure 2, but with the velocity computed by evaluating the Biot-Savart integral.

In the numerical implementation, all integrals over non-singular elements on the right-hand side of (4.14) are computed using a triangle quadrature. Over the singular elements, the first and third integrals on the right-hand side are computed using the polar integration rule described at the beginning of this section for the vector potential. The mean curvature κ_m is computed from the second fundamental form of the surface by differentiating with respect to local triangle barycentric coordinates. Over the flat elements supporting a curved triangle, the mean curvature is assumed to be constant and equal to the mean curvature at the centroid of the curved triangle.

To assess the accuracy of the method, we repeated the computations described earlier for uniform flow past a stationary sphere represented by a vortex sheet. Figure 3 shows the x-component of the principal velocity at the marker points for three levels of discretization. According to the exact solution, the data should fall on a sinusoidal curve with amplitude $0.75U$. For the third level of discretization corresponding to 512 boundary elements, the maximum relative error is on the order of 0.1%. Comparing these results to those shown in figure 2, we find that, for a coarse discretization, the indirect method of computing the velocity by differentiating the principal value of the potential is superior. At higher resolutions, the performances of the two methods are comparable.

An alternative method of evaluating the Biot-Savart integral was proposed recently by Zinchenko, Rother & Davis (1999) and discussed further by Pozrikidis (2000*b*). Using a series of vector identities, we find the following counterpart of expression (4.14):

$$\begin{aligned} \boldsymbol{u}^{PV}(\boldsymbol{x}_0) = \boldsymbol{u}^{\infty}(\boldsymbol{x}_0) + \tfrac{1}{2}\boldsymbol{\zeta}(\boldsymbol{x}_0) \times \boldsymbol{n}(\boldsymbol{x}_0) - \int_D \nabla G(\boldsymbol{x}, \boldsymbol{x}_0) \times [\boldsymbol{\zeta}(\boldsymbol{x}) - \boldsymbol{\zeta}(\boldsymbol{x}_0)]\, \mathrm{d}S(\boldsymbol{x}) \\ + \boldsymbol{\zeta}(\boldsymbol{x}_0) \times \int_D \{[\boldsymbol{n}(\boldsymbol{x}_0)\, \boldsymbol{n}(\boldsymbol{x}) + \boldsymbol{n}(\boldsymbol{x})\, \boldsymbol{n}(\boldsymbol{x}_0)] \cdot \nabla G(\boldsymbol{x}, \boldsymbol{x}_0) \\ + [1 - \boldsymbol{n}(\boldsymbol{x}_0) \cdot \boldsymbol{n}(\boldsymbol{x})]\ \nabla G(\boldsymbol{x}, \boldsymbol{x}_0)\}\, \mathrm{d}S(\boldsymbol{x}). \end{aligned} \tag{4.15}$$

The second integral on the right-hand side of (4.15) involves a nonsingular but multi-valued integrand that may be integrated over curved elements with sufficient accuracy using a triangle quadrature. The importance of accounting for the curvature of the vortex sheet is once again apparent: the second integral on the right-hand side of (4.15) evaluated at a point over a flat element hosting the point is identically equal to zero. Test computations for a spherical vortex sheet have shown that the accuracy associated with (4.15) is comparable to that of the generalized vortex method. We found, however, that expression (4.14) allows for more robust dynamical simulations.

The results shown in figures 2 and 3 are representative of smooth shapes where the position of the nodes and circulation field are specified to machine precision. During a dynamical simulation, numerical error introduces fluctuations in the circulation field, strength of the vortex sheet, and position of the marker points. Numerical differentiation of the vector potential and principal value of the harmonic potential in the tangential plane amplify the noise and thus degrade the performance of the indirect method. In contrast, performing the Biot-Savart integral effectively smoothes out the fluctuations.

Analogous equations can be derived for singly and doubly periodic vortex sheets. In the case of a doubly periodic vortex sheet, the Green's function discussed in Appendix A satisfies the identity

$$\int_D^{PV} \boldsymbol{n}(\boldsymbol{x}) \cdot \nabla G^{3D-2P}(\boldsymbol{x}, \boldsymbol{x}_0) \, \mathrm{d}S(\boldsymbol{x}) = 0. \tag{4.16}$$

Accordingly, equations (4.13) and (4.14) hold with D identified with one period of the vortex sheet, but the second term on the right-hand sides is absent.

5. Numerical simulations

The numerical methods described in the §§ 3 and 4 were implemented in a computer program that is able to simulate the self-induced motion of closed or doubly periodic vortex sheets separating two fluids with equal density, corresponding to vanishing Atwood ratio, $A = 0$. An assortment of simulations were carried out to study the performance of the numerical methods, compare the effectiveness of formulations based on the time integration of the evolution equation for the jump in velocity across the vortex sheet or distribution of the circulation, and compare the performance of the indirect and direct method for evaluating the Biot-Savart integral. In this section, we discuss representative results of simulations for three prototypical configurations.

In the simulations, the non-singular integrals over quadratic triangles were computed by the seven-point triangle quadrature, and the singular integrals were computed by the six-point double Gauss–Legendre quadrature (e.g. Pozrikidis 1998). Time integration was carried out by the explicit first- or second-order Euler method, with a sufficiently small time step. In the simulations presented in this section, the marker points move with the principal velocity of the vortex sheet. The change in the volume enclosed by a closed vortex sheet was less than 0.1% for the duration of each simulation. A complete run for a closed vortex sheet requires several hours of CPU time on an INTEL 550 MHz personal computer rulling LINUX with the g77 FORTRAN compiler. A complete run of a doubly-periodic vortex sheet requires five times as much CPU time due to the expensive evaluation of the doubly periodic Laplace Green's function discussed in Appendix A.

5.1. *Deformation of a released spherical vortex sheet*

Consider streaming flow with velocity U past a sphere of radius a, and regard the surface of the sphere as a stationary vortex sheet whose induced velocity cancels the normal component of the velocity of the incident flow to satisfy the no-penetration boundary condition. At the origin of time, the interior of the sphere is assumed to be filled by a fluid whose density is equal to that of the exterior fluid, and the sphere is deformed into an ellipsoid. Even without initial deformation, convection of vorticity toward the rear stagnation point causes the spherical vortex sheet to deform under the influence of its self-induced velocity, while the flow and the shape of the vortex sheet remain axisymmetric.

Figure 4 shows sequences of evolving profiles in a meridional plane of an initially spherical vortex, computed with 512 elements defined by 1026 marker points, using the second-order Euler method with time step $\Delta t = 0.01\ a/U$. Panels (*a–d*) correpond to simulations based on alternative problem formulations, as will be discussed in the next paragraph. In all cases, the instantaneous strength of the vortex sheet is computed by requiring conservation of the circulation, as mandated by (3.20) for vanishing surface tension. Integrating in time the evolution equation for the jump in the velocity, equation (3.12) with $A = 0$ and $T = 0$, yielded results that are indistinguishable within plotting resolution.

In the simulations shown in figure 4(*a, b*), the marker point velocity is computed, respectively, indirectly according to the generalized vortex method or directly by evaluating the Biot-Savart integral. The motion is regular for a limited period of time, but numerical instabilities set in over the rear and upper portion of the vortex sheet at later times where the vortex sheet is expected to roll up into an axisymmetric spiral. The instability in the position of the marker points over a three-dimensional vortex sheet is the counterpart of the sawtooth instability reported in previous simulations for two-dimensional flow. The present numerical results suggest that the direct method of evaluating the Biot-Savart integral is somewhat better than the generalized vortex method.

One way to regularize the motion is to replace the distance $|\boldsymbol{x} - \boldsymbol{x}_0|$ in the denominator of the free-space Green's function in the Biot-Savart kernel with the modified distance $(|\boldsymbol{x} - \boldsymbol{x}_0|^2 + a^2\delta^2)^{1/2}$, where δ is a dimensionless smoothing parameter introduced by Krasny (1986*b*) for two-dimensional flow. In figure 4(*c, d*), we present sequences of evolving profiles for $\delta^2 = 0.01$ and 0.02. The instability is suppressed, with the penalty that the fine geometrical features of the motion are sensitive to the value of smoothing parameter δ^2, in agreement with the findings of previous authors. These simulations ended when the grid was no longer able to represent the deformed vortex sheet with adequate resolution. In figure 4(*e, f*), we present three-dimensional views of the deformed vortex at an advanced evolution stage for $\delta^2 = 0.02$, showing the severe deformation of the interfacial elements and demonstrating the need for regridding.

Figure 5(*a*) shows the initial shape of an oblate spheroidal vortex sheet that is axially symmetric about the z-axis, arising by deforming the spherical vortex sheet while preserving the circulation at the marker points. The ratio of the initial spheroid axes in the directions of the z- and x-axes is 3/4. Figure 5(*b*) shows the shape of the vortex sheet at time $t = 1.5\ a/U$, after the vortex sheet has deformed under the influence of its self-induced velocity, computed with $\delta^2 = 0.02$. Important features of the motion are the development of a cavity at the rear of the vortex sheet, and the simultaneous ejection of a vortex tail. Severe stretching of the elements causes the simulation to end at the time corresponding to figure 5(*b*).

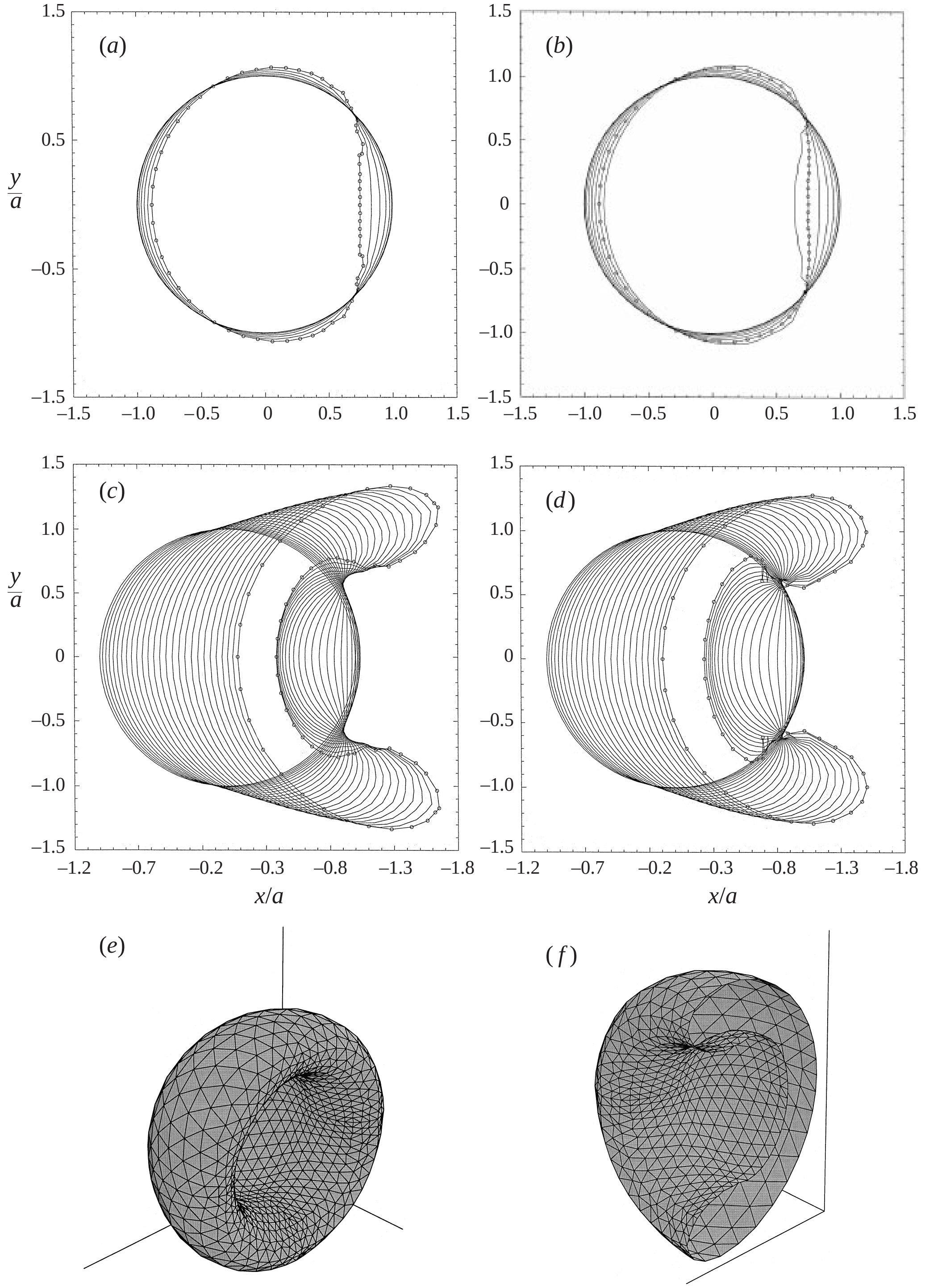

FIGURE 4. (a–d) Sequences of evolving profiles in a meridional plane of an initial spherical vortex sheet, computed with 512 elements, at dimensionless times $ta/U = 0, 0.2, 0.3, \ldots$: ($a$) unregularized motion computed by the generalized vortex method; (b–d) motion computed by directly evaluating the Biot-Savart integral with $\delta = 0, 0.01, 0.02$. (d, f) Three-dimensional perspectives of the shape of the vortex sheet at the end of the simulation with $\delta^2 = 0.02$.

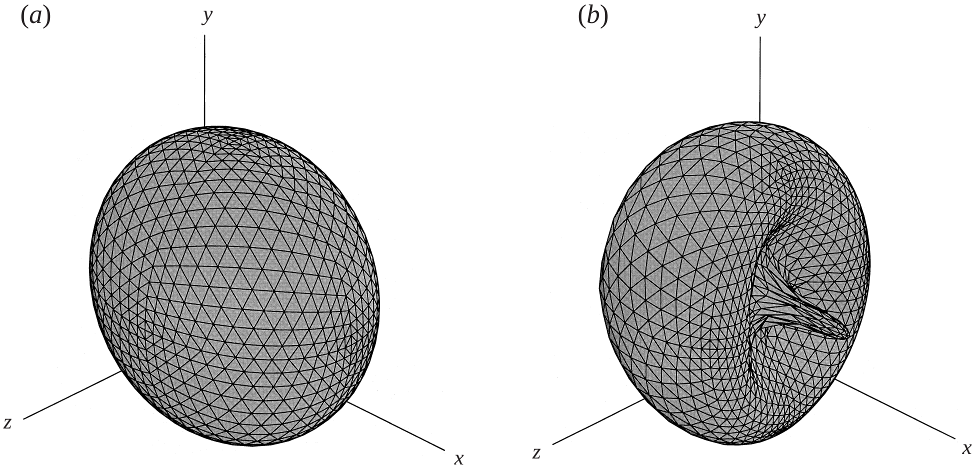

FIGURE 5. Three-dimensional perspectives of (a) the initial and (b) an advanced stage in the evolution of an initially oblate spheroidal vortex sheet that arises by deforming the sphere while preserving the circulation at the marker points.

Additional simulations were carried out to study the effect of surface tension. When surface tension is dominant, a spherical vortex sheet remains nearly stationary, exhibiting only mild deformation. In this case, best results are obtained when the marker points are required to move with the velocity of the fluid normal to the vortex sheet, so that the surface grid is nearly stationary. Unfortunately, at large values of surface tension, a prohibitively small time step is required to prevent numerical instabilities, and the motion could be followed only for a limited period of time.

5.2. *Oscillations of inviscid drops induced by surface tension*

In a second case study, we consider the surface-tension-induced oscillations of a neutrally buoyant inviscid drop suspended in an ambient inviscid fluid of infinite expanse. Lamb (1932) studied the linearized motion and found that, in spherical polar coordinates (r, θ, φ), the radius of a nearly spherical drop exhibiting small-amplitude normal-mode oscillations is described by

$$r = a\ [1 + \epsilon\ T_j^{|m|}(\cos\theta)\cos(m\varphi)\sin(\omega_j t)] \tag{5.1}$$

for $j > 2$ and $m = 0, \pm 1, \pm 2, \ldots, \pm j$, where a is the radius of the undeformed drop, ϵ is a dimensionless number whose magnitude is small compared to unity, and ω_j is the angular frequency of the oscillations. In the case of a neutrally buoyant drop,

$$\omega_j = \sqrt{\frac{T}{\rho a^3}\ \frac{(j-1)j(j+1)(j+2)}{2j+1}}. \tag{5.2}$$

The modified Legendre functions of degree j and order m on the right-hand side of (5.1) are given by

$$T_j^{|m|}(\cos\theta) = \frac{1}{2}\sqrt{\frac{2j+1}{\pi}}\ \sqrt{\frac{(j-|m|)!}{(j+|m|)!}}\ P_j^{|m|}(\cos\theta) \tag{5.3}$$

where $P_j^{|m|}(\cos\theta)$ are the associated Legendre functions; $P_j^0(\cos\theta)$ are the jth-degree Legendre polynomials (e.g. Korn & Korn 1961). The complex functions $\Phi_j^m \equiv T_j^{|m|}(\cos\theta)\exp(-\mathrm{i}m\varphi)$, where i is the imaginary unit, comprise an orthogonal set. Using expressions for the potential provided by Lamb (1932), we find that the circulation of the vortex sheet associated with the velocity discontinuity across the drop surface is given by

$$\Gamma(\theta,\varphi) \equiv \phi^+ - \phi^- = -\epsilon\ \omega_j\ a^2\ \frac{2j+1}{j(j+1)}\ T_j^{|m|}(\cos\theta) \tag{5.4}$$

where the superscripts + and − denote, respectively, the exterior and interior side. The total energy of the flow consists of the surface energy due to surface tension given by $E_S = T\ S_D$, where S_D is the instantaneous drop surface area, and the kinetic energy of the interior and exterior flow denoted by E_K. For fluids of equal density, the kinetic energy may be expressed as an integral in terms of the circulation,

$$E_K = -\tfrac{1}{2}\ \rho \int_D \Gamma\ \boldsymbol{n}\cdot\nabla\phi\ \mathrm{d}S. \tag{5.5}$$

In the absence of viscous dissipation, the total energy $E_T = E_S + E_K$ is an invariant of the motion.

Figure 6 shows results of numerical simulations for the axisymmetric mode $j = 2$, $m = 0$, where the drop oscillates between a prolate and an oblate shape, both axially symmetric around the x-axis, for a moderate but non-infinitesimal amplitude $\epsilon = 0.10$. Figure 6(*a*) displays the evolution of the x semi-axis of the drop denoted by a_x, reduced by the radius of the spherical drop a, plotted against the reduced dimensionless time $\hat{t} \equiv t\sqrt{\rho a^3/T}$. The solid and dotted lines correspond to simulations where the velocity is computed directly from the Biot-Savart integral with $\delta^2 = 0$ or 0.01; the dashed, long-dashed, and dot-dashed lines correspond to simulations where the velocity is computed using the generalized vortex method, respectively, with $\delta^2 = 0$ or 0.02, or with the circulation field smoothed after 20 times steps of size $\Delta t = 0.01\sqrt{\rho a^3/T}$. Smoothing of the circulation field was effected by expanding it in surface harmonics over the undeformed sphere, and then truncating the expansion to eliminate the high-frequency components, as discussed by Pozrikidis (2000*a*). According to linear theory, the drop oscillates with period equal to $2.868\sqrt{\rho a^3/T}$, and the amplitude of the oscillation is equal to $0.063078a$, corresponding to the vertical and horizontal straight lines in figure 6(*a*).

At small times, the computed nonlinear motion is in good agreement with the predictions of linear theory, but all simulations develop incurable numerical instabilities after a certain period of evolution. The longest surviving simulation corresponds to the generalized vortex method with periodic smoothing of the circulation field. Even this simulation, however, suffers from incurable numerical instabilities that could not be eliminated even when the coordinates of the marker points were smoothed by spectrum truncation. Figure 6(*b*) shows the evolution of the reduced surface energy, $\hat{E}_S \equiv E_S/(4\pi T a^2)$, reduced kinetic energy, $\hat{E}_K \equiv E_S/(4\pi T a^2)$, and reduced total energy $\hat{E} = \hat{E}_S + \hat{E}_K$. The smooth behaviour at small times validates the numerical method and suggests that if numerical instabilities did not arise, the simulation would have preserved the total energy within the error expected due to the spatial discretization. Similar results were obtained for non-axisymmetric modes.

Pozrikidis (2000*a*) successfully simulated the surface-tension-induced oscillations of inviscid drops suspended in a zero-density ambient fluid, corresponding to Atwood ratio of unity. His simulations were conducted using a generalized vortex method in which the surface distribution of the potential is updated using Bernoulli's equation

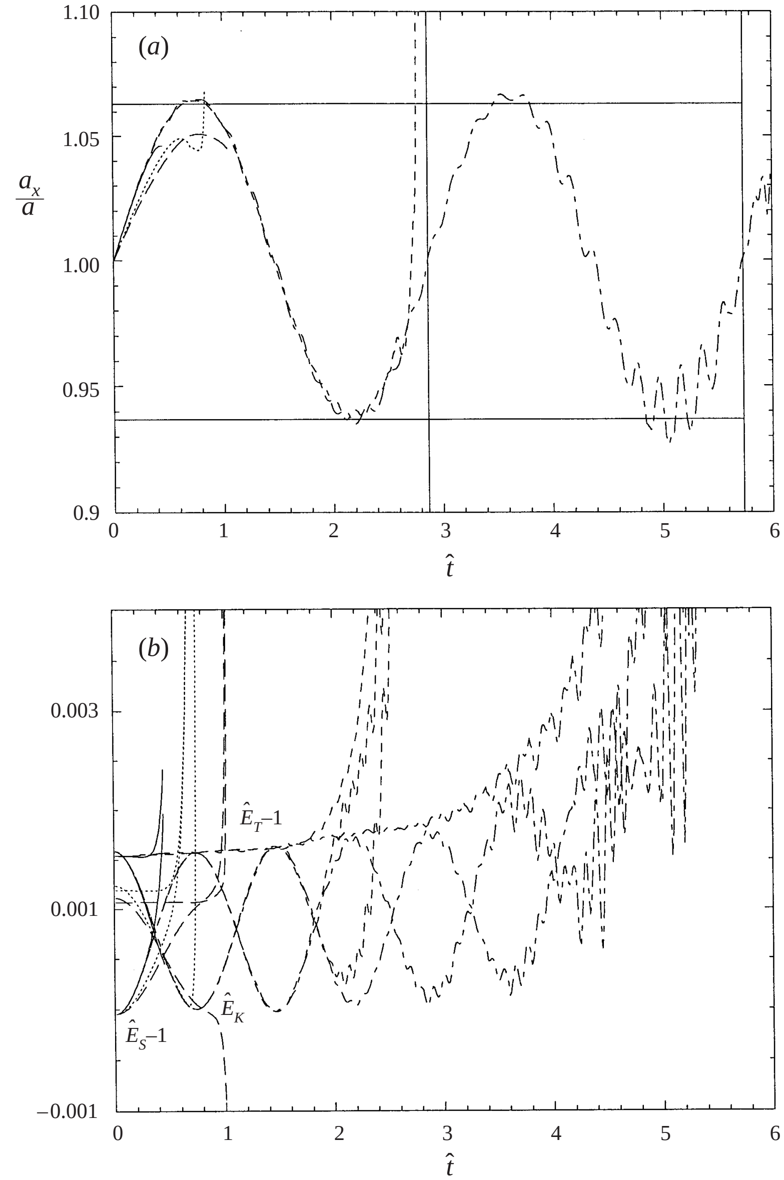

FIGURE 6. (*a*) Oscillations of the x semi-axis of the drop computed by several methods, as described in the text; (*b*) correponding oscillations of the surface, kinetic, and total energy of the flow.

for the interior flow, and the surface circulation is computed by solving an integral equation. Periodic smoothing of the potential over the free surface was sufficient for eliminating irregularities, and allowed the motion to be described for an indefinite period of time. The present simulations reveal the occurrence of more severe instabilities for zero value of the Arwood ratio in a surface-tension-induced flow.

5.3. *Kelvin–Helmholtz instability of a doubly periodic vortex sheet*

Next, we turn our attention to a doubly periodic vortex sheet embedded in a homogeneous fluid. When the vortex sheet is flat and parallel to the (x, y)-plane,

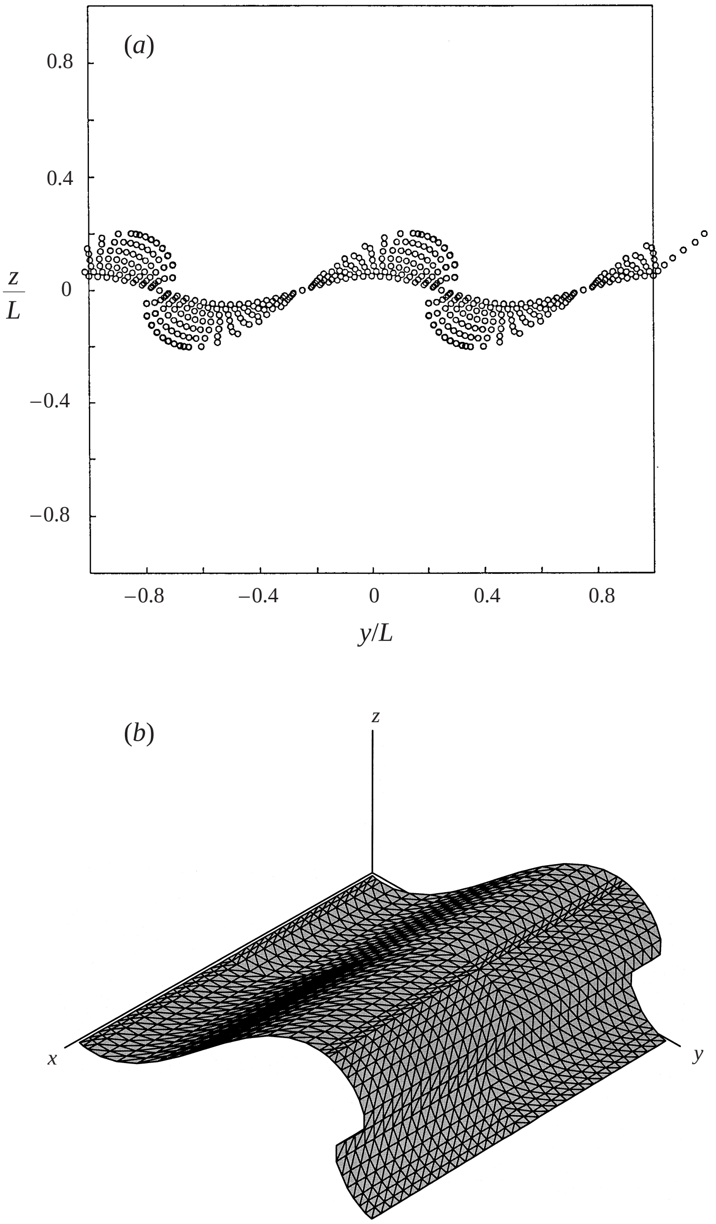

FIGURE 7. (*a*) Stages in the Kelvin–Helmholtz instability of a vortex sheet subject to a normal-mode two-dimensional perturbation, computed with $\delta^2 = 0.02$. The circles mark the positions of marker points. (*b*) A three-dimensional view corresponding to the last instant shown in (*a*).

and its strength sheet ζ is uniform, we obtain a surface of discontinuity separating two adjacent steams with different uniform velocities. Small perturbations initiate the Kelvin–Helmholtz instability leading to periodic roll-up, as described by numerous previous authors. The analytic structure of the vortex sheet subject to two-dimensional perturbations, and the spontaneous formation of a geometrical singularity discovered by Moore (1979) have been studied extensively by analytical and numerical methods (e.g. Cowley, Baker & Tanveer 1999).

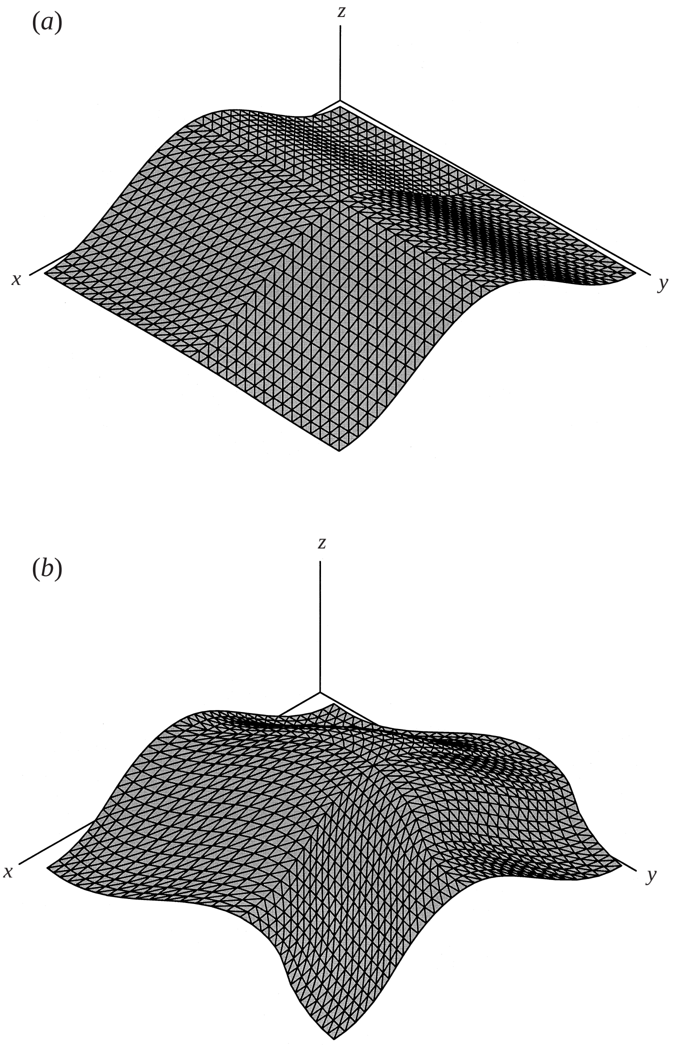

FIGURE 8. (*a*) The initial, and (*b*) an advanced stage in the evolution of a doubly periodic vortex sheet subject to a three-dimensional perturbation.

In the numerical studies, the motion of the vortex sheet is computed subject to generally three-dimensional perturbations. In the simulations, one period of the vortex sheet is discretized into 512 elements defined by 1090 marker points. To confirm the consistency of the method, the motion of a vortex sheet was first simulated subject to small-amplitude two-dimensional normal-mode perturbations with wavenumber vectors perpendicular to the strength of the vortex sheet, and excellent agreement was confirmed with the growth rates predicted by linear stability theory. In the absence of regularization, sawtooth instabilities develop, as observed in previous simulations of two-dimensional flow using the point vortex method and higher-order discretizations. As in the case of a closed vortex sheet discussed in § 5.1, the instabilities may be suppressed by regularizing the Biot-Savart kernel using Krasny's (1986*b*) modification.

Figure 7(*a*) shows a sequence of profiles of a perturbed vortex sheet in the (y, z)-

plane, at dimensionless times $tU/L = 0, 0.12, 0.24, \ldots$, computed with $\delta^2 = 0.02$; U is the magnitude of the velocity far above and below the vortex sheet, and L is the wavelength of the perturbation. Regularization was effected by replacing the distance $|\boldsymbol{x} - \boldsymbol{x}_0|$ in the denominator of the most singular term of the real-space sum of the doubly periodic Green's function with the modified distance $(|\boldsymbol{x} - \boldsymbol{x}_0|^2 + L^2\delta^2)^{1/2}$ (Appendix A). Each one of the circles in figure 7(*a*) is a superposition of a group of circles marking the position of corresponding element nodes over one period in the spanwise direction. The nearly perfect superposition confirms that the computed flow remains two-dimensional. The motion was followed up to the point where the interfacial grid failed to describe the motion with sufficient accuracy, and the simulation failed. Figure 7(*b*) shows a three-dimensional view of the rolled-up sheet illustrating the element distribution at an advanced stage of the motion.

Figure 8(*a, b*) shows the initial and an advanced stage in the evolution of an infinite vortex sheet subject to a doubly periodic perturbation corresponding to the orthogonal base vectors $\boldsymbol{a}_1 = L(1, 0, 0)$ and $\boldsymbol{a}_2 = L(0, 1, 0)$, directed along the x- or y-axes, computed with $\delta^2 = 0.02$. At the initial instant, the amplitude of the marker point displacement in the streamwise or spanwise directions is equal, respectively, to $0.005L$ and $0.10L$, where the spanwise disturbance is superposed on a normal-mode two-dimensional perturbation. The evolution leads to formation of corrugated spanwise structures observed in previous simulations of shear flow, but the motion could not be computed at long times without compromising the accuracy due to insufficient spatial resolution.

6. Discussion

We have derived and discussed equations governing the self-induced motion of closed and periodic three-dimensional vortex sheets; we have developed numerical methods for computing the principal value of the Biot-Savart integral without regularizing the kernel; and we have implemented a method for simulating the motion of vortex sheets using standard boundary-element discretization. Numerical simulations have shown that the methods successfully describe the motion of vortex sheets for a limited period of time, up to the point where numerical instabilities dominate. Previous experience with two-dimensional vortex sheets suggests that the time when the computations break down may be delayed by reducing the interpolation error using a large number of marker points or elements, by reducing the integration error using high-order quadratures, and by carrying out the computations in extended precision. In principle, these improvements may also be applied to the case of three-dimensional flow. In practice, however, the computational cost is so high that only special cases can be considered.

We have found that when the motion of a vortex sheet evolving in a homogeneous fluid is regularized using Krasny's method, the motion in the absence of surface tension may be followed up to the point where the grid becomes so distorted that the motion may no longer be described with sufficient resolution. In the presence of surface tension, or when the densities of the fluids on either side of the vortex sheet are not equal, kernel regularization alone may not be sufficient for filtering out numerical instabilities, and direct smoothing by diffusion or spectrum truncation may be necessary (Kerr 1988, Pozrikidis 2000*a*). An effective method of smoothing the position of marker points defining the triangulation has not been developed.

Even with regularization and smoothing implemented, adaptive triangulation according to local curvature is necessary for continuing the simulations at long times and for capturing roll-up. Brady *et al.* (1998) mapped sections of a vortex sheet onto a planar rectangle in parametric space, and regridded in the plane using error estimates based on the square of the mean curvature. Their simulations typically start with a number of triangles on the order of 10^3, and end with a number of triangles on the order of 10^5. Kwak & Pozrikidis (1998) used the advancing front method to adaptively regrid directly in physical space according to the local or mean directional curvature, thereby circumventing the need for mapping. Combining the advancing front method with the methods developed in this work is under current development. Even with an efficient adaptive method for regridding implemented, the spontaneous development of fine scales in vortex sheet dynamics requires exceedingly large computer memory storage and computing time, and this is a main practical concern in performing simulations for an extended period of time.

Moore (1979) discovered, and subsequent researchers confirmed, that a singularity in curvature spontaneously occurs during the Kelvin–Helmholtz instability of a two-dimensional vortex sheet after a finite evolution time. Ishihara & Kaneda (1994, 1995) used perturbation expansions to study the development of a singularity on a three-dimensional vortex sheet subject to doubly periodic perturbations. Their results provided evidence for loss of the analyticity at a critical time, but the nature of the singularity could not be described. The numerical methods developed in this work provide a means for probing the nature of the singularity following, for example, the approach of Krasny (1986*a*). This investigation will be pursued in a future study.

This research is supported by a grant provided by NASA.

Appendix A. Computation of the doubly periodic Green's function of Laplace's equation

We consider the computation of the doubly periodic Green's function of Laplace's equation in three dimensions, denoted by G^{3D-2P}, satisfying the equation $\nabla^2 G^{3D-2P} + \sum \delta(\boldsymbol{x}-\boldsymbol{x}_n) = 0$, where δ is the three-dimensional delta function, and the summation is over all singular points located at $\boldsymbol{x}_n = \boldsymbol{x}_0 + \boldsymbol{X}_n$; $\boldsymbol{x}_0$ is the position of an arbitrary singular point, and the vectors $\boldsymbol{X}_n$ define the vertices of a two-dimensional lattice located at

$$\boldsymbol{X}_n = i_1\, \boldsymbol{a}_1 + i_2\, \boldsymbol{a}_2 \qquad \text{(A 1)}$$

where i_1 and i_2 are two integers, and $\boldsymbol{a}_1$ and $\boldsymbol{a}_2$ are two unit base vectors parallel to the $(1,2)$- or (x,y)-plane, as shown in figure 1(*c*). Physically, the Green's function represents the harmonic potential due to a doubly periodic array of point sinks with negative unit strength. As the field point $\boldsymbol{x}$ moves far above or below the (x,y)-plane, the Green's function exhibits the asymptotic behaviour $G^{3D-2P} \simeq -|z|/(2A_c)$, where $A_c = |\boldsymbol{a}_1 \times \boldsymbol{a}_2|$ is the area of one unit cell.

To compute the periodic Green's function, we introduce the reciprocal wavenumber base vectors

$$\boldsymbol{b}_1 = \frac{2\pi}{A_c}\, \boldsymbol{a}_2 \times \boldsymbol{e}_z, \qquad \boldsymbol{b}_2 = \frac{2\pi}{A_c}\, \boldsymbol{e}_z \times \boldsymbol{a}_1, \qquad \text{(A 2)}$$

where $\boldsymbol{e}_z$ is the unit vector along the z-axis, and define the vertices of the reciprocal wavenumber lattice

$$\boldsymbol{l}_\lambda = j_1\, \boldsymbol{b}_1 + j_2\, \boldsymbol{b}_2 \qquad \text{(A 3)}$$

where j_1 and j_2 are two integers. Using the method of Fourier transform, we find that the Green's function is given by

$$G^{3D-2P}(\boldsymbol{x},\boldsymbol{x}_0)=\frac{1}{2A_c}\left[-|\hat{\boldsymbol{x}}_0\cdot\boldsymbol{e}_z|+\sum_{\lambda}\frac{1}{|\boldsymbol{l}_\lambda|}\cos(\boldsymbol{l}_\lambda\cdot\hat{\boldsymbol{x}}_0)\exp(-|\boldsymbol{l}_\lambda|\,|\hat{\boldsymbol{x}}_0\cdot\boldsymbol{e}_z|)\right] \tag{A 4}$$

where $\hat{\boldsymbol{x}}_n\equiv\boldsymbol{x}-\boldsymbol{x}_n$ is the distance of the field point $\boldsymbol{x}$ from the nth singular point $\boldsymbol{x}_n$. The zero wavenumber is excluded from the summation on the right-hand side of (A 4).

Expression (A 4) is useful only when the field point $\boldsymbol{x}$ is located sufficiently far from the plane of the singularities, for then the exponential factors multiplying the cosines decay at a fast rate. As the observation point approaches the plane of the singularities, the accurate evaluation of the Fourier series requires an increasing number of terms; and when the observation lies in the plane of the singularities, the summation fails.

Several attempts have been made by previous authors to compute the Green's function in terms of Ewald sums (Baker *et al.* 1984; Sangani & Behl 1989). We find that an indirect method developed by Hautman & Klein (1992) in the context of molecular electrostatics is the best approach. Adapted to the present context, the method involves defining the projection of the field point $\boldsymbol{x}$ onto the plane of the singularities, denoted by $\boldsymbol{s}$, and introducing the distance of the projection from a singular point $\boldsymbol{x}_n$, defined as $\hat{\boldsymbol{s}}_n\equiv\boldsymbol{s}-\boldsymbol{x}_n$. The Green's function is computed in five parts using the exact decomposition

$$G^{3D-2P}(\boldsymbol{x},\boldsymbol{x}_0)=-\frac{1}{2A_c}|\hat{\boldsymbol{x}}_0\cdot\boldsymbol{e}_z|+\frac{1}{4\pi}[R(\boldsymbol{x},\boldsymbol{x}_0)+S_0(\boldsymbol{s})-\tfrac{1}{2}|\hat{\boldsymbol{x}}_0\cdot\boldsymbol{e}_z|^2\,S_1(\boldsymbol{s})+\tfrac{3}{8}|\hat{\boldsymbol{x}}_0\cdot\boldsymbol{e}_z|^4\,S_2(\boldsymbol{s})] \tag{A 5}$$

where

$$R(\boldsymbol{x},\boldsymbol{x}_0)\equiv\sum_n\left[\frac{1}{|\hat{\boldsymbol{x}}_n|}-\frac{1}{|\hat{\boldsymbol{s}}_n|}+\frac{1}{2}\frac{|\hat{\boldsymbol{x}}_0\cdot\boldsymbol{e}_z|^2}{|\hat{\boldsymbol{s}}_n|^3}-\frac{3}{8}\frac{|\hat{\boldsymbol{x}}_0\cdot\boldsymbol{e}_z|^4}{|\hat{\boldsymbol{s}}_n|^5}\right] \tag{A 6}$$

and the summation is over all singular points. The summed terms on the right-hand side of (A 6) decay like $1/|\hat{\boldsymbol{s}}|^7$, and this expedites the numerical computation. When, in particular, the observation point $\boldsymbol{x}$ lies in the plane of the singularities, $R(\boldsymbol{x},\boldsymbol{x}_0)$ is identically equal to zero and its evaluation is not required. More generally, the indices i_1 and i_2 introduced in (A 1) for summing in the plane of the singularities on the right-hand side of (A 6), may be truncated at an appropriate level that depends on the distance of the evaluation point from the plane of the singularities. The three new functions on the right-hand side of equation (A 5) are computed from the Ewald decompositions

$$\left.\begin{aligned}
S_0(\boldsymbol{s})&=\sum_n\frac{1-H_0(\xi|\hat{\boldsymbol{s}}_n|)}{|\hat{\boldsymbol{s}}_n|}+\frac{2\pi}{A_c}\left[-\frac{1}{\sqrt{\pi}\xi}+\sum_\lambda\frac{1}{|\boldsymbol{l}_\lambda|}\cos(\boldsymbol{l}_\lambda\cdot\hat{\boldsymbol{s}}_0)\,\mathrm{erfc}\left(\frac{|\boldsymbol{l}_\lambda|}{2\xi}\right)\right],\\
S_1(\boldsymbol{s})&=\sum_n\frac{1-H_1(\xi|\hat{\boldsymbol{s}}_n|)}{|\hat{\boldsymbol{s}}_n|^3}-\frac{2\pi}{A_c}\sum_\lambda|\boldsymbol{l}_\lambda|\cos(\boldsymbol{l}_\lambda\cdot\hat{\boldsymbol{s}}_0)\,\mathrm{erfc}\left(\frac{|\boldsymbol{l}_\lambda|}{2\xi}\right),\\
S_2(\boldsymbol{s})&=\sum_n\frac{1-H_2(\xi|\hat{\boldsymbol{s}}_n|)}{|\hat{\boldsymbol{s}}_n|^5}-\frac{2\pi}{A_c}\frac{1}{9}\sum_\lambda|\boldsymbol{l}_\lambda|^3\cos(\boldsymbol{l}_\lambda\cdot\hat{\boldsymbol{s}}_0)\,\mathrm{erfc}\left(\frac{|\boldsymbol{l}_\lambda|}{2\xi}\right),
\end{aligned}\right\} \tag{A 7}$$

where erfc is the complementary error function, ξ is a Ewald summation parameter determining the balance between the sums in real and wavenumber space on the right-hand sides of expressions (A 7), and the zero wavenumber is excluded from the second sums involving the cosines. The splitting functions H_0, H_1, and H_2 involved in the real-space sums are given by

$$\left.\begin{aligned} &H_0(w) = \operatorname{erf}(w), \qquad H_1(w) = \operatorname{erf}(w) - \frac{2}{\sqrt{\pi}}\, w(1+2w^2)\exp(-w^2), \\ &H_2(w) = \operatorname{erf}(w) - \frac{2}{\sqrt{\pi}}\, w(1+\tfrac{2}{3}w^2 - \tfrac{4}{9}w^4 + \tfrac{8}{9}w^6)\exp(-w^2), \end{aligned}\right\} \tag{A 8}$$

where erf is the error function. The Gaussian decay of these functions, combined with the Gaussian decay of the complementary error function on the right-hand sides of (A 7), is a key to the efficiency of the numerical method. The results are, and have been confirmed to be, independent of the splitting parameter ξ, with the optimal value for the least amount of computational effort depending on the lattice geometry. In practice, with the optimal choice, the indices i_1 and i_2 defined in equation (A 1) for summing in real space, and the indices j_1 and j_2 defined in equation (A 3) for summing in wavenumber space, are truncated at a moderate level between 2 and 5.

The second method of computing the Green's function is useful when a field point is located near, or lies in, the plane of the singularities. As the field point moves far from the plane of the singularities, the Fourier series method described earlier becomes more efficient.

Appendix B. Proof of identity (3.17)

Consider a system of surface curvilinear coordinates (ξ, η) defined over the surface of an evolving three-dimensional vortex sheet, as shown in figure 1. In terms of the circulation $\varGamma$, the jump in the tangential velocity across the vortex sheet is given by

$$\Delta \boldsymbol{u} = \frac{1}{1-\beta^2}\left[\left(\frac{1}{h_\xi}\,\frac{\partial \varGamma}{\partial \xi} - \beta\,\frac{1}{h_\eta}\,\frac{\partial \varGamma}{\partial \eta}\right)\boldsymbol{t}_\xi + \left(\frac{1}{h_\eta}\,\frac{\partial \varGamma}{\partial \eta} - \beta\,\frac{1}{h_\xi}\,\frac{\partial \varGamma}{\partial \xi}\right)\boldsymbol{t}_\eta\right] \tag{B 1}$$

where $\boldsymbol{t}_\xi$ and $\boldsymbol{t}_\eta$ are the unit vectors along the ξ- or η-axis, h_ξ and h_η are the corresponding metric coefficients, and $\beta = \boldsymbol{t}_\xi \cdot \boldsymbol{t}_\eta$. To simplify the proof, we assume that at a particular time instant, the surface curvilinear coordinates are locally orthogonal corresponding to $\beta = 0$, but do not necessarily remain orthogonal, that is, $\mathrm{d}\beta/\mathrm{d}t \neq 0$. Differentiating (B 1) following the motion of the marker points, we find

$$\begin{aligned} \frac{\mathrm{d}\Delta \boldsymbol{u}}{\mathrm{d}t} = \frac{1}{h_\xi}\frac{\partial \varGamma}{\partial \xi}\,\frac{\mathrm{d}\boldsymbol{t}_\xi}{\mathrm{d}t} + \left[\frac{\mathrm{d}}{\mathrm{d}t}\left(\frac{1}{h_\xi}\,\frac{\partial \varGamma}{\partial \xi}\right) - \frac{\mathrm{d}\beta}{\mathrm{d}t}\,\frac{1}{h_\eta}\,\frac{\partial \varGamma}{\partial \eta}\right]\boldsymbol{t}_\xi \\ +\frac{1}{h_\eta}\,\frac{\partial \varGamma}{\partial \eta}\,\frac{\mathrm{d}\boldsymbol{t}_\eta}{\mathrm{d}t} + \left[\frac{\mathrm{d}}{\mathrm{d}t}\left(\frac{1}{h_\eta}\,\frac{\partial \varGamma}{\partial \eta}\right) - \frac{\mathrm{d}\beta}{\mathrm{d}t}\,\frac{1}{h_\xi}\,\frac{\partial \varGamma}{\partial \xi}\right]\boldsymbol{t}_\eta. \end{aligned} \tag{B 2}$$

Next, we invoke the evolution laws for the rate of change of the length of a material vector (e.g. Pozrikidis 1997, Chap. 1), and find the following expressions:

$$\left.\begin{aligned} &\frac{\mathrm{d}\boldsymbol{t}_\xi}{\mathrm{d}t} = \boldsymbol{t}_\xi \cdot (\nabla \boldsymbol{u}^{PV}) \cdot (\boldsymbol{I} - \boldsymbol{t}_\xi\,\boldsymbol{t}_\xi), \qquad \frac{\mathrm{d}\boldsymbol{t}_\xi}{\mathrm{d}t} = \boldsymbol{t}_\eta \cdot (\nabla \boldsymbol{u}^{PV}) \cdot (\boldsymbol{I} - \boldsymbol{t}_\eta \boldsymbol{t}_\eta), \\ &\frac{\mathrm{d}}{\mathrm{d}t}\left(\frac{1}{h_\eta}\frac{\partial \varGamma}{\partial \xi}\right) = \frac{1}{h_\xi}\,\frac{\partial}{\partial \xi}\left(\frac{\mathrm{d}\varGamma}{\mathrm{d}t}\right) - \frac{1}{h_\xi}\,\frac{\partial \varGamma}{\partial \xi}\,\boldsymbol{t}_\xi \cdot (\nabla \boldsymbol{u}^{PV}) \cdot \boldsymbol{t}_\xi, \\ &\frac{\mathrm{d}}{\mathrm{d}t}\left(\frac{1}{h_\eta}\frac{\partial \varGamma}{\partial \eta}\right) = \frac{1}{h_\eta}\,\frac{\partial}{\partial \eta}\left(\frac{\mathrm{d}\varGamma}{\mathrm{d}t}\right) - \frac{1}{h_\eta}\,\frac{\partial \varGamma}{\partial \eta}\,\boldsymbol{t}_\eta \cdot (\nabla \boldsymbol{u}^{PV}) \cdot \boldsymbol{t}_\eta. \end{aligned}\right\} \tag{B 3}$$

Working in a similar manner, under the assumption that the tangential field of the principal velocity is irrotational, we find

$$\frac{\mathrm{d}\beta}{\mathrm{d}t} = 2\boldsymbol{t}_\eta \cdot (\nabla \boldsymbol{u}^{PV}) \cdot \boldsymbol{t}_\xi + 2\boldsymbol{t}_\xi \cdot (\nabla \boldsymbol{u}^{PV}) \cdot \boldsymbol{t}_\eta. \tag{B 4}$$

Substituting relations (B 3) and (B 4) into (B 2), we obtain

$$\begin{aligned}\frac{\mathrm{d}\Delta\boldsymbol{u}}{\mathrm{d}t} &= \frac{1}{h_\xi}\frac{\partial}{\partial\xi}\left(\frac{\mathrm{d}\Gamma}{\mathrm{d}t}\right) + \frac{1}{h_\eta}\frac{\partial}{\partial\eta}\left(\frac{\mathrm{d}\Gamma}{\mathrm{d}t}\right) \\ &\quad + \left(\frac{1}{h_\xi}\frac{\partial\Gamma}{\partial\xi}\,\boldsymbol{t}_\xi + \frac{1}{h_\eta}\frac{\partial\Gamma}{\partial\eta}\,\boldsymbol{t}_\eta\right)\cdot(\nabla\boldsymbol{u}^{PV})\cdot(\boldsymbol{I} - 2\boldsymbol{t}_\xi\boldsymbol{t}_\xi - 2\boldsymbol{t}_\eta\boldsymbol{t}_\eta)\end{aligned} \tag{B 5}$$

which implies (3.17).

REFERENCES

Agishtein, M. E. & Migdal, A. A. 1989 Dynamics of vortex surfaces in three dimensions: theory and simulations. *Physica* D **40**, 91–118.

Baker, G. R. 1983 Generalized vortex methods for free-surface flows. In *Waves on Fluid Interfaces* (ed. R. E. Meyer). Academic.

Baker, G. R., Meiron, D. I. & Orszag, S. A. 1984 Boundary integral methods for axisymmetric and three-dimensional Rayleigh-Taylor instability problems. *Physica* **12D**, 19–31.

Baker, G. R., Meiron, D. I. & Orszag, S. A. 1982 Generalized vortex methods for free-surface flow problems. *J. Fluid Mech.* **123**, 477–501.

Baker, G. R. & Moore, D. W. 1989 The rise and distortion of a two-dimensional gas bubble in an inviscid fluid. *Phys. Fluids* A **1**, 1451–1459.

Brady, M., Leonard, A. & Pullin, D. I. 1998 Regularized vortex sheet evolution in three dimensions. *J. Comput. Phys.* **146**, 520–545.

Caflisch, R. E. 1988 Mathematical analysis of vortex dynamics. In *Mathematical Aspects of Vortex Dynamics, SIAM Proc.* (ed. R. E. Caflish), pp. 1–24.

Caflisch, R. E. & Li, X. 1992 Lagrangian theory for 3D vortex sheets with axial or helical symmetry. *Transport Theory Statist. Phys.* **21**, 559–578.

Caflisch, R. E., Li, X. & Shelley, M. J. 1993 The collapse of an axi-symmetric, swirling vortex sheet. *Nonlinearity* **6**, 843–867.

Cowley, S. J., Baker, G. R. & Tanveer, S. 1999 On the formation of Moore curvature singularities in vortex sheets. *J. Fluid Mech.* **378**, 233–267.

Haroldsen, D. J. & Meiron, D. I. 1998 Numerical calculation of three-dimensional interfacial potential flows using the point vortex method. *SIAM J. Sci. Comput.* **20**, 648–683.

Hautman, J. & Klein, M. L. 1992 An Ewald summation method for planar surfaces and interfaces. *Molecular Phys.* **75**, 379–395.

Ishihara, T. & Kaneda, Y. 1994 Spontaneous singularity formation in the shape of a vortex sheet three-dimensional flow. *J. Phys. Soc. Japan* **63**, 388–392.

Ishihara, T. & Kaneda, Y. 1995 Singularity formation in three-dimensional motion of a vortex sheet. *J. Fluid Mech.* **300**, 339–366.

Kaneda, Y. 1990 A representation of the motion of a vortex sheet in a three-dimensional flow. *Phys. Fluids* A **2**, 458–461.

Kerr, R. M. 1988 Simulation of Rayleigh–Taylor flows using vortex blobs. *J. Comput. Phys.* **76**, 48–84.

Korn, G. A. & Korn, T. M. 1961 *Mathematical Handbook for Scientists and Engineers.* McGraw Hill.

Krasny, R. 1986*a* A numerical study of singularity formation in a vortex sheet by the point vortex method. *J. Fluid Mech.* **167**, 65–93.

Krasny, R. 1986*b* Desingularization of the periodic vortex sheet roll up. *J. Comp. Phys.* **65**, 292–312.

Kwak, S. & Pozrikidis, C. 1998 Adaptive triangulation of evolving, closed or open surfaces by the advancing-front method. *J. Comput. Phys.* **145**, 61–88.

Lamb, H. 1932 *Hydrodynamics*. Cambridge University Press.

Leonard, A. 1985 Computing three-dimensional incompressible flows with vortex elements. *Ann. Rev. Fluid Mech.* **17**, 523–529.

Lozano, A., Garcìa-Olivares, A. & Dopazo, C. 1998 The instability growth leading to a liquid sheet breakup. *Phys. Fluids* **10**, 2188–2197.

Moore, D. W. 1979 The spontaneous appearance of a singularity in the shape of an evolving vortex sheet. *Proc. R. Soc. Lond.* A **365**, 105–119.

Pozrikidis, C. 1997 *Introduction to Theoretical and Computational Fluid Dynamics*. Oxford University Press.

Pozrikidis, C. 1998 *Numerical Computation in Science and Engineering*. Oxford University Press.

Pozrikidis, C. 2000*a* Three-dimensional oscillations of inviscid drops induced by surface tension. *Computers Fluids*, In Press.

Pozrikidis, C. 2000*b* Interfacial dynamics for Stokes flow. *J. Comput. Phys.*, In Press.

Puckett, E. G. 1993 Vortex methods: An introduction and survey of selected research topics. In *Incompressible Fluid Dynamics: Trends and Advances* (ed. M. D. Gunzburger & R. A. Nicolaides). Cambridge University Press.

Rosenhead, L. 1931 The formation of vortices from a surface of discontinuity. *Proc. R. Soc. Lond.* A **134**, 170–192.

Saffman, P. G. 1992 *Vortex Dynamics*. Cambridge University Press.

Sangani, A. S. & Behl, S. 1989 The planar singular solutions of Stokes and Laplace equations and their application to transport processes near porous surfaces. *Phys. Fluids* A **1**, 21–37.

Shelley, M. J. 1992 A study of singularity formation in vortex-sheet motion by a spectrally accurate vortex method. *J. Fluid Mech.* **244**, 493–526.

Wu, J.-Z. 1995 A theory of three-dimensional interfacial vorticity dynamics. *Phys. Fluids* **7**, 2375–2395.

Zinchenko, A. Z., Rother, M. A. & Davis, R. H. 1999 Cusping, capture and breakup of interacting drops by a curvatureless boundary-integral algorithm. *J. Fluid Mech.* **391**, 249–292.